Neurobiology of Disease

Blocking Site-Specific Cleavage of Human Tau Delays Progression of Disease-Related Phenotypes in Genetically Matched Tau-Transgenic Mice Modeling Frontotemporal Dementia

Elizabeth L. Steuer,[1,2]* **Lisa J. Kemper,**[1,2]* **Chris J.W. Hlynialuk,**[1,2] **Kailee Leinonen-Wright,**[1,2] **Michelle L. Montonye,**[1,2] **Ian P. Lapcinski,**[1,2] Colleen L. Forster,[1,3] **Karen H. Ashe,**[1,2,4] **and Peng Liu**[1,2]

[1]N. Bud Grossman Center for Memory Research and Care, [2]Department of Neurology, [3]UMN Academic Health Center Biological Materials Procurement Network, University of Minnesota, Minneapolis, Minnesota 55455, and [4]Geriatric Research, Education, and Clinical Centers, Veterans Affairs Medical Center, Minneapolis, Minnesota 55417

Studies have recently demonstrated that a caspase-2-mediated cleavage of human tau (htau) at asparate-314 (D314) is responsible for cognitive deficits and neurodegeneration in mice modeling frontotemporal dementia (FTD). However, these animal studies may be confounded by flaws in their model systems, such as endogenous functional gene disruption and inequivalent transgene expression. To avoid these weaknesses, we examined the pathogenic role of this site-specific htau cleavage in FTD using genetically matched htau targeted-insertion mouse lines: rT2 and rT3. Both male and female mice were included in this study. rT2 mice contain a single copy of the FTD-linked htau proline-to-leucine mutation at amino acid 301 (htau P301L), inserted into a neutral site to avoid dysregulation of host gene expression. The similarly constructed rT3 mice harbor an additional D314-to-glutamate (D314E) mutation that blocks htau cleavage. We demonstrate that htau transgene expression occurs primarily in the forebrain at similar levels in rT2 and rT3 mice. Importantly, expression of the cleavage-resistant D314E mutant delays transgene-induced tau accumulation in the postsynaptic density, brain atrophy, hippocampal neurodegeneration, and spatial memory impairment, without altering age-related progression of pathologic tau conformation and phosphorylation. Our comprehensive investigation of age-dependent disease phenotypes associated with the htau P301L variant in precisely engineered FTD-modeling mice unveils a transiently protective effect of blocking htau cleavage at D314. Findings of this study advance our understanding of the contribution of this tau cleavage to the pathogenesis of FTD, and aid the development of effective dementia-targeting therapies.

Key words: cognition; dementia; microtubule-associated protein tau; mouse model; neurodegeneration; synapse

---

Significance Statement

A site-specific and caspase-2-mediated cleavage of human tau plays a pathologic role in dementia. In this study, we investigate the contribution of this cleavage to the pathogenesis of frontotemporal dementia (FTD) using two genetically matched, tau-transgene targeted-insertion mouse lines that differ only by a cleavage-resistant mutation. The use of these mice avoids confounding effects associated with the random integration of tau transgenes to the mouse genome and allows us to comprehensively evaluate the impact of the tau cleavage on FTD phenotypes. Our data reveal that blocking this tau cleavage delays memory impairment and neurodegeneration of FTD-modeling mice. These findings improve our understanding of the pathogenic mechanisms underlying FTD and will facilitate the development of effective therapeutics.

Introduction

Tau is a highly soluble and interactive neuronal protein that undergoes a multitude of post-translational modifications to maintain cell homeostasis. When these modifications are dysregulated, various morphologies of tau inclusions can accumulate, this pathologic hallmark spans a heterogeneous group of neurodegenerative disorders collectively known as tauopathies. The discovery of >90 naturally occurring tau variants in cases of frontotemporal dementia (FTD) (Alzforum; https://www.alzforum.org/mutations/mapt) suggests a key pathologic role of dysregulated tau, but the mechanisms underlying this etiology are not fully understood.

Site-specific cleavage of human tau (htau) by caspase-2 (Casp2) at aspartate-314 (D314, 2N4R htau numbering) generates Δtau314 (Zhao et al., 2016), a soluble tau species that is relevant to multiple tauopathies (Zhao et al., 2016; Liu et al., 2019, 2020; Smith et al., 2019). Previous findings (Zhao et al., 2016) suggest that Casp2-mediated htau cleavage at D314 induces cognitive impairment and hippocampal degeneration in both rTg4510 and adeno-associated virus (AAV)-induced FTD model systems. rTg4510 mice (Ramsden et al., 2005; Santacruz et al., 2005) harbor an htau transgene that contains a proline-to-leucine mutation at amino acid 301 (htau P301L) linked to frontotemporal dementia and parkinsonism linked to chromosome 17 (Dumanchin et al., 1998; Hutton et al., 1998). AAV-mediated hippocampal transfection of WT mice induces expression of cleavage-sensitive htau P301L or cleavage-resistant htau P301L D314E (an aspartate-to-glutamate mutation at amino acid 314). However, the aforementioned models present several problematic and confounding variables that obscure research findings. First, the random insertion of ~70 copies of the tau transgene during the generation of Tg4510 responder mice disrupts *fibroblast growth factor 14* (*Fgf14*) (Gamache et al., 2019; Goodwin et al., 2019). Fibroblast growth factor 14 protein is involved in neurotransmitter signaling, synaptic plasticity, and cognitive function (Xiao et al., 2007; Alshammari et al., 2016; Di Re et al., 2017). As such, the dysregulation of *Fgf14* may alter some observed effects of tau transgene expression on rTg4510 disease phenotypes. Second, the steady-state protein levels of AAV-transfected htau P301L and htau P301L D314E were unequal in these mice (Zhao et al., 2016). More broadly, AAV-mediated gene delivery models present several obstacles: Transgene expression levels are difficult to control, limited vector packaging capacity can cause a loss of transgene expression pattern specificity (Cook-Snyder et al., 2015), and the host genome can be disrupted by the integration of AAV transgenes (Deyle and Russell, 2009). Together, these shortcomings invite a need for more precisely engineered models of FTD.

In the present studies, we examine the impact of site-specific htau cleavage at D314 on cognitive function and neuropathology using two novel mouse lines: rT2 and rT3. The rT2 and rT3 mice harbor a single copy of the htau P301L and the htau P301L D314E transgene, respectively. These transgenes were inserted in a neutral site known to promote transgene expression without dysregulating endogenous gene expression (Beard et al., 2006). We demonstrate that (1) the htau transgenes are expressed primarily in the forebrain and at a similar level between rT2 and rT3 mice, (2) the site-specific htau cleavage occurring in rT2 mice is blocked by the D314E mutation in rT3 mice, (3) the onset of spatial memory impairment in rT2 mice is delayed but not prevented in rT3 mice, (4) spatial memory impairment in rT2 and rT3 mice coincides with excessive htau accumulation and de-anchoring of AMPARs in the postsynaptic density (PSD), (5) brain atrophy and hippocampal neurodegeneration begins at older ages in rT3 than in rT2 mice, and (6) age-related progression of pathologic tau conformation and phosphorylation is similar in rT2 and rT3 mice. Overall, these findings support a pathogenic role for site-specific htau cleavage at D314 in FTD and increase our understanding of tau-related disease mechanisms. The presently characterized mouse model system can be used as a tool for preclinical assessment of therapies targeting this cleavage.

Materials and Methods

Generation of rT2 and rT3 mice. The bigenic rT2 and rT3 mice were generated by crossing the activator CaMKIIα-tetracycline-controlled transactivator (tTA) line (Mayford et al., 1996) to responder FVB-T2 (harboring a P301L variant of htau transgene (*MAPT*)) and FVB-T3 (harboring an additional D314E mutation of the *MAPT* P301L variant) line, respectively.

To generate T2 responder mice, a single-copy transgene integration strategy mediated by site-specific recombination was adopted. First, ES cell lines were engineered to carry a tetracycline response element (TRE)-controlled *MAPT* P301L variant based on a procedure previously described (Gamache et al., 2019). Specifically, 25 μg of purified plasmid Col1a-frt-hygro-pA (Addgene) was transfected by electroporation into v6.5 Mouse ES cells (passage #22, Novus Biologicals) derived from a male of C57BL/6 × 129/sv background. The incorporation of an "Flp-in" integration cassette of the plasmid into the genomic sequence downstream of collagen, Type I, α1 (*Col1A1*) was accomplished by homologous recombination (see Fig. 1). Properly engineered ES cells were selected by their resistance to the aminoglycoside antibiotic G418. The DNA sequence of engineered cells was verified, and their karyotypes were assessed. Clone 15 (v6.5Col1A1#15) was identified to have an accurately integrated exogenous DNA sequence and a normal karyotype. All further flippase recognition target (*FRT*)-mediated targeting was performed in this modified ES cell line.

The *MAPT* P301L variant sequence contained a TRE promoter sequence, the mouse prion protein gene (*prnp*) encoding partial introns 1 and 2 plus exons 2 and 3, the cDNA open reading frame encoding the isoform containing four microtubule-binding domains but no amino-terminal inserts (0N4R), and an SV40 poly(A) signal sequence. This sequence was cloned from a plasmid (pTRE.prnp.tau$_{P301L}$) that was used to generate Tg4510 responder mice (Santacruz et al., 2005) and then inserted downstream of the frt 3′-end in the plasmid pgk-ATG-frt (Addgene) containing an "Flp-in" promoter cassette; 6 μg of the resulting DNA construct and 0.5 μg of an eighth generation flippase (FLP) protein (FLPe) transient expression vector pCAGGS-FLPe (Gene Bridges) containing DNA sequence that encodes FLP recombinase were cotransfected into the v6.5Col1A1#15 ES cell line (see Fig. 1). Hygromycin (140 μg/ml) was used to select ES clones resistant to the antibiotic. Accurate DNA recombination and clone selection for *MAPT* P301L variant sequence were verified, and the karyotype of these cells was examined using detailed methods previously published (Gamache et al., 2019, 2020). T2 responder mice were generated by injecting the properly engineered, *MAPT* P301L variant-containing ES cells into host blastocysts. The responder mice were back-crossed 5 times to FVB WT mice to obtain *MAPT* P301L-hemizygous T2 mice and were maintained on an FVB/N background.

T3 responder mice were similarly generated, except that an additional D314E mutation of the *MAPT* P301L variant was introduced to the engineered plasmid pgk-ATG-frt.

The activator mice harbor an engineered tTA transgene (*CKtTA*) whose specific forebrain neuron expression is driven by a modified *CaMKIIα* promoter (Mayford et al., 1996). *CKtTA*-hemizygous activator mice were maintained on a 129S6 background.

Female responder mice were bred to male activator mice to generate F1 experimental cohorts (htau$^{+/-}$ tTA$^{+/-}$). Littermates with htau$^{-/-}$ tTA$^{+/-}$ or htau$^{-/-}$ tTA$^{-/-}$ genotypes were used as controls.
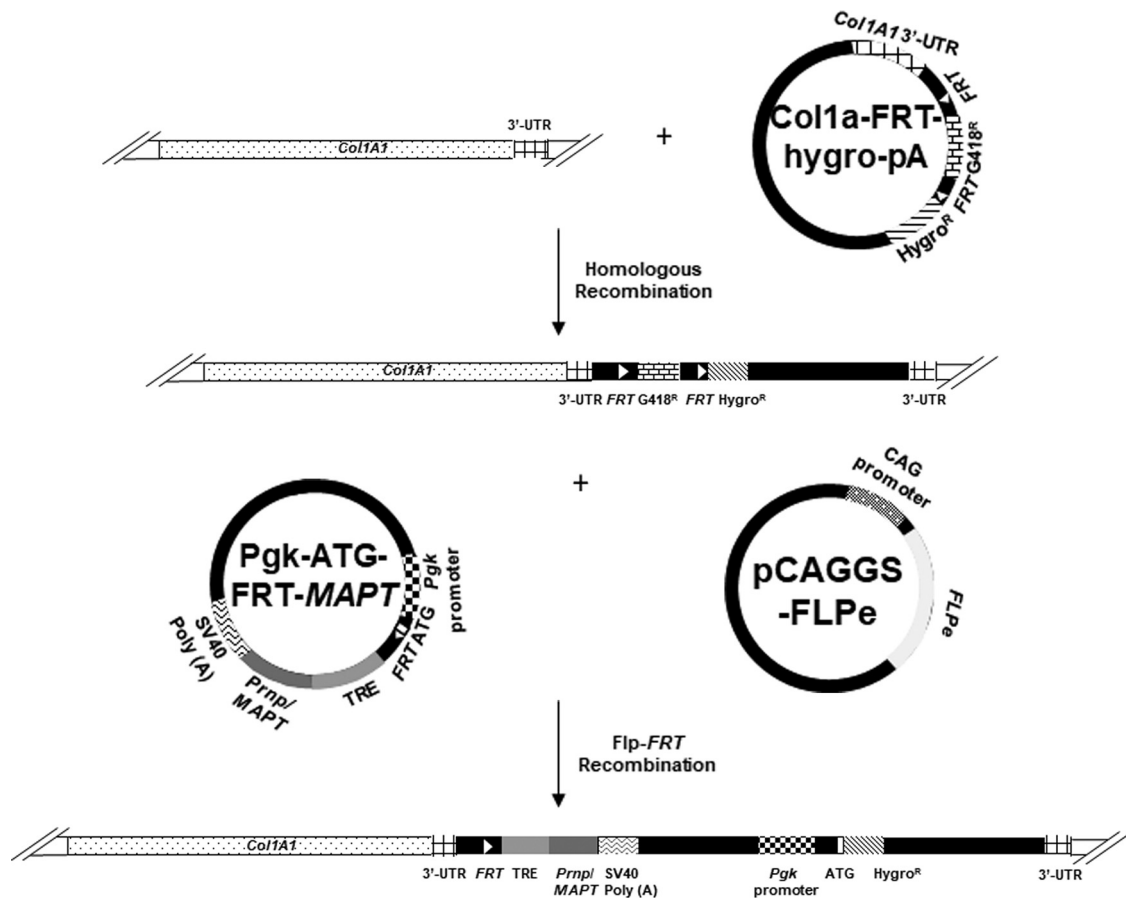
Figure 1. Engineering *MAPT* transgenes in responder mouse lines: A schematic illustration. *Col1A1*, collagen; Type I, α1 gene; 3'-UTR, the three prime untranslated region; G418[R], an open reading frame encoding aminoglycoside phosphotransferase from the Tn5 transposon that confers resistance to geneticin; *FRT*, flippase (FLP) recognition target; Hygro[R], an open reading frame encoding aminoglycoside phosphotransferase from *E. coli* that confers resistance to hygromycin; *Pgk* promoter, the mouse phosphoglycerate kinase 1 promoter; ATG, the start codon; *Prnp/ MAPT*, DNA sequence encoding the 0N4R isoform of human tau inserted in the mouse prion protein gene encoding partial introns 1 and 2 plus exons 2-3; SV40 poly(A), simian virus 40 poly-adenylation tail; CAG promoter, a synthetic promoter engineered from the cytomegalovirus early enhancer element, the chicken β-actin promoter, and the splice acceptor of the rabbit β-globin gene; *FLPe*, an open reading frame encoding a fusion between simian virus 40 nuclear localization signal and the *S. cerevisiae* site-specific recombinase FLP.

The bigenic rT1 mice harboring nonmutant (i.e., WT) *MAPT* were also used in this study. Detailed generation and characterization of rT1 mice were reported previously (Gamache et al., 2020).

Mice. Experiments involving mice were conducted in full accordance with the guidelines of the Association for Assessment and Accreditation of Laboratory Animal Care and approved by the Institutional Animal Care and Use Committee at the University of Minnesota (approval #2012-38712A). Mice of both genders were used in experiments, and statistical analyses showed no significant ($p > 0.05$) gender effects.

Mice were anesthetized with isoflurane (nose cone/vaporizer flow rate 3%) and killed by decapitation. Tissue specimens of interest were immediately harvested and processed after death. For immunofluorescence experiments examining neurodegeneration, following anesthetization and before death, mice were transcardially perfused with ice-cold 1× PBS (pH 7.4) followed by 4% (w/v) PFA (dissolved in 1× PBS, final pH 6.9). For all the other studies using tissue specimens, anesthetized mice were transcardially perfused with ice-cold 1× PBS (pH 7.4) before death.

mRNA ISH. The spatial expression pattern of transgenic *MAPT* mRNA in the brains of rT2 and rT3 mice (Table 1; see Fig. 2A) was revealed using a commercially available BaseScope RED assay (ACDBio). Specifically, 2-month-old rT2 mice were used; age- and gender-matched, transgenic littermates expressing only tTA were used as a negative control for *MAPT* expression. The same experimental design was applied to rT3 mice. The left hemisphere was dissected and fixed in 4% (w/v) PFA at 4°C for 5 d. The fixed tissue was then embedded in paraffin, processed as 5-μm-thick sagittal sections, and mounted on charged microscope slides. mRNA ISH was performed according to the

manufacturer's instructions using a probe (ACDBio, catalog #702311) that targets a *MAPT* mRNA sequence spanning exons 12 and 13 (5'-GGCTCAUUAGGCAACAUCCAUCAUAAACCAGGAGGUGGCCA-GG-3'). To map the spatial expression pattern of *MAPT* mRNA, brain sections were scanned using a TissueScope LE slide scanner (Huron Digital Pathology) at the University of Minnesota Imaging Centers (UIC, RRID:SCR_020997).

RNA extraction. To isolate total RNA, 2-month-old rT2 and rT3 mice and their respective, age- and gender-matched transgenic littermates expressing only tTA were used (Table 1; see Fig. 3A). The forebrain (whole-brain ridding cerebellum, brainstem, and olfactory bulb) of the left hemisphere was first homogenized using a MagNA Lyser instrument (Roche Diagnostics). Tissue specimens and MagNA Lyser green beads (Roche Diagnostics) were agitated at 6,500 rpm (rotation speed), room temperature (RT), for 50 s in 1 ml of precooled Qiazol reagent supplied with an RNeasy lipid tissue mini kit (QIAGEN). Total RNA was then isolated using the kit according to the manufacturer's instructions. The RNA concentration and purity were determined using a DU 730 Life Science UV/Vis Spectrophotometer (Beckman Coulter). The RNA integrity was determined by assessing the relative intensities of 28S and 18S rRNA electrophoresed in 1% (w/v) agarose gels.

qRT-PCR. In order to compare mRNA expression levels of *MAPT* transgenes in the rT2 and rT3 mice, RT-qPCR was performed in two steps: cDNA synthesis and real-time PCR. First, 5 μg of isolated RNA samples was treated with RNase-free DNase I (New England Biolabs) according to the manufacturer's instructions to eliminate DNA contamination. Next, single-stranded cDNA of *MAPT*

Table 1. Mice used in this study

| | | Mouse line | | | | | | | |
| | | rT1 | | rT2 | | | rT3 | | |
Figure	Age (mo)	htau$^{+/-}$ tTA$^{+/-}$	htau$^{-/-}$ tTA$^{-/-}$	htau$^{+/-}$ tTA$^{+/-}$	htau$^{-/-}$ tTA$^{+/-}$	htau$^{-/-}$ tTA$^{-/-}$	htau$^{+/-}$ tTA$^{+/-}$	htau$^{-/-}$ tTA$^{+/-}$	htau$^{-/-}$ tTA$^{-/-}$
2	2	n.a.	n.a.	1F 1M	1F 1M	n.a.	1F 1M	1F 1M	n.a.
3A	2	n.a.	n.a.	2F 3M	n.a.	n.a.	2F 4M	n.a.	n.a.
3B	2	n.a.	n.a.	3F 5M	n.a.	n.a.	2F 4M	n.a.	n.a.
3C	2	n.a.	n.a.	3F 5M	4F 4M	n.a.	3F 4M	5F 4M	n.a.
4	5-9	n.a.	n.a.	5F 4M	n.a.	1F 1M	4F 4M	n.a.	1F 1M
5A,B–D	5	n.a.	n.a.	6F 6M	n.a.	6F 6M	n.a.	n.a.	n.a.
5A,E–G	5	n.a.	n.a.	n.a.	n.a.	n.a.	6F 6M	n.a.	6F 6M
5A,H–J	8	n.a.	n.a.	8F 8M	n.a.	8F 8M	n.a.	n.a.	n.a.
5A,K–M	8	n.a.	n.a.	n.a.	n.a.	n.a.	8F 8M	n.a.	8F 8M
5A,N–P	12	n.a.	n.a.	6F 6M	n.a.	6F 6M	n.a.	n.a.	n.a.
5A,Q–S	12	n.a.	n.a.	n.a.	n.a.	n.a.	6F 6M	n.a.	3F 6M
6	5	3F 3M	1F 1M	4F 2M	n.a.	1F	3F 3M	n.a.	1F 2M
6	8	4F 2M	1F 1M	1F 3M	n.a.	1F 1M	3F 3M	n.a.	1F 1M
6	12	4F 2M	2M	6F 3M	n.a.	1F 1M	3F 3M	n.a.	2F
6	15	2F 2M	2F	2F 4M	n.a.	1F 1M	4F 2M	n.a.	1F 1M
6	18	2F 2M	1F 1M	2F 2M	n.a.	1F 1M	2F 2M	n.a.	1F 1M
7A,B	5	4F 4M	1F 1M	6F 2M	n.a.	1F 1M	4F 4M	n.a.	3F 1M
7A,B	8	3F 2M	1F 1M	7F 4M	n.a.	3F 1M	4F 4M	n.a.	3F 1M
7A,B	12	8F 4M	1F 4M	10F 5M	n.a.	5F 2M	4F 3M	n.a.	2F 2M
7A,B	15	2F 2M	2F 1M	3F 3M	n.a.	2F 2M	4F 2M	n.a.	2F 2M
7A,B	18	2F 2M	1F 1M	2F 2M	n.a.	2F 2M	2F 2M	n.a.	1F 1M
8B	5	2F 2M	n.a.	3F 2M	n.a.	n.a.	3F 2M	n.a.	n.a.
8B	8	3F 1M	n.a.	2F 3M	n.a.	n.a.	3F 3M	n.a.	n.a.
8B	12	3F 2M	n.a.	3F 2M	n.a.	n.a.	1F 3M	n.a.	n.a.
8B	15	2F 2M	n.a.	2F 2M	n.a.	n.a.	3F 1M	n.a.	n.a.
8A,B	18	2F 2M	n.a.	2F 2M	n.a.	n.a.	2F 2M	n.a.	n.a.
8C	5	3F 3M	n.a.	4F 2M	n.a.	n.a.	3F 3M	n.a.	n.a.
8C	8	2F 1M	n.a.	2F 3M	n.a.	n.a.	2F 3M	n.a.	n.a.
8C	12	2F 2M	n.a.	3F 3M	n.a.	n.a.	2F 2M	n.a.	n.a.
8C	15	2F 2M	n.a.	2F 2M	n.a.	n.a.	3F 1M	n.a.	n.a.
8A,C	18	2F 2M	n.a.	2F 2M	n.a.	n.a.	2F 2M	n.a.	n.a.
8D	5	2F 3M	n.a.	3F 2M	n.a.	n.a.	3F 2M	n.a.	n.a.
8D	8	3F 1M	n.a.	2F 2M	n.a.	n.a.	3F 1M	n.a.	n.a.
8D	12	6F 2M	n.a.	6F 2M	n.a.	n.a.	2F 3M	n.a.	n.a.
8D	15	2F 2M	n.a.	2F 2M	n.a.	n.a.	3F 2M	n.a.	n.a.
8A,D	18	2F 2M	n.a.	2F 2M	n.a.	n.a.	2F 2M	n.a.	n.a.
8E	5	2F 2M	n.a.	2F 2M	n.a.	n.a.	2F 2M	n.a.	n.a.
8E	8	3F 1M	n.a.	2F 1M	n.a.	n.a.	3F 1M	n.a.	n.a.
8E	12	6F 2M	n.a.	6F 3M	n.a.	n.a.	2F 3M	n.a.	n.a.
8E	15	2F 2M	n.a.	2F 2M	n.a.	n.a.	2F 2M	n.a.	n.a.
8A,E	18	2F 2M	n.a.	2F 2M	n.a.	n.a.	2F 2M	n.a.	n.a.
9	5	n.a.	n.a.	2F 3M	n.a.	3F 3M	5F 2M	n.a.	3F 3M
9	8	n.a.	n.a.	5F 5M	n.a.	3F 3M	5F 5M	n.a.	3F 3M
9	12	n.a.	n.a.	4F 5M	n.a.	3F 3M	5F 1M	n.a.	2F 3M

mo = months of age, F = female(s), M = male(s), n.a. = not applicable.

was synthesized from 250 ng of DNase I-treated RNA using an iScript cDNA synthesis kit (Bio-Rad) following the manufacturer's instructions. Finally, real-time PCR was conducted using a LightCycler 480 (Roche Applied Sciences), as previously described in detail (Gamache et al., 2020). Briefly, mRNA of the *MAPT* transgene was quantified by normalizing to that of an endogenous reference gene, hypoxanthine phosphoribosyltransferase 1 (*Hprt1*), using SYBR Green I as the DNA-binding fluorescence dye. The following primers were used for real-time PCR: *MAPT* forward, 5′-CTACACCATGCACCAAGACC-3′; *MAPT* reverse, 5′-TGCTTTTACT GACCATGCGA-3′; *Hprt1* forward, 5′-GCTGGTGAAAAGGACCTCT-3′; and *Hprt1* reverse, 5′-CCACAGGACTAGAACACCTGCTA-3′. Experimenters performing RT-qPCR were blind to mouse genotype.

Protein extraction. To explore the spatial expression pattern of transgenic htau protein, to compare the expression levels of htau, and to determine the levels of htau relative to those of endogenous murine tau (mtau) in rT2 and rT3 mice, a one-step protein extraction procedure

was used as previously described (Liu et al., 2011) with minor modifications.

To explore the spatial expression pattern of htau (Table 1; see Fig. 2B), 2-month-old rT2 mice were used; age- and gender-matched, transgenic littermates expressing only tTA were used as a negative control for htau expression. The same experimental design was applied to rT3 mice. The olfactory bulb, hippocampus, cerebral cortex, cerebellum, and brainstem of the right hemisphere, and the spinal cord were isolated. Tissue specimens were mechanically homogenized in extraction buffer (50 mM Tris-HCl, pH 7.4; 150 mM NaCl; 1 mM EGTA; 0.3% (w/v) SDS; 1% (w/v) deoxycholate; 0.5% (v/v) polyethylene glycol p-(1,1,3,3-tetramethylbutyl)-phenyl ether (Triton X-100); 0.1 mM PMSF; 0.2 mM 1,10-phenanthroline monohydrate; a protease inhibitor cocktail (Millipore Sigma); and two phosphatase inhibitor cocktails (Millipore Sigma; and Santa Cruz Biotechnology). Tissue homogenates were gently agitated on a rotator at 4°C for 1 h and then centrifuged (16,100 $\times$ g) at 4°C for

Figure 2. Spatial expression pattern of htau transgenes in rT2 and rT3 mice. ***A***, Representative ISH photomicrographs showing mRNA expression of htau transgenes (indicated by red signals) in sagittal sections of 2-month-old rT2 and rT3 mice. Scale bar, 0.8 mm. ***B***, Representative SWAWB images showing protein expression of htau transgenes in six distinct anatomic regions of the CNS of 2-month-old rT2 and rT3 mice: olfactory bulb (Olf.), cerebral cortex (Ctx.), hippocampus (Hippo.), cerebellum (Cbm.), brainstem (Br. St.), and spinal cord (Sp. C.). Top, fl-htau revealed using monoclonal htau-specific HT7 antibody. Bottom, Total brain proteins. htau P301L$^{+/-}$ tTA$^{+/-}$, rT2 mice; htau P301L D314E$^{+/-}$ tTA$^{+/-}$, rT3 mice; htau P301L$^{-/-}$ tTA$^{+/-}$ and htau P301L D314E$^{-/-}$ tTA$^{+/-}$: age-matched littermates of rT2 and rT3 mice, respectively, that expressed only the tTA activator. These mice served as negative controls. The expression pattern of htau transgenes was similar in both genders, and only that of female mice is shown. kDa, kilodaltons.

was homogenized in 5 volumes of ice-cold extraction buffer (25 mM Tris-HCl, pH 7.4; 140 mM NaCl; and 3 mM KCl with the protease and phosphatase inhibitors described above) using a Dounce homogenizer (PolyScience) at the highest speed for 25 strokes. The resulting material was centrifuged at 16,100 × g, 4°C for 90 min. The supernatant was subsequently depleted of endogenous IgG and stored at −80°C.

Protein concentration was determined by a BCA assay (Thermo Fisher Scientific) according to the manufacturer's instructions.

Subcellular fractionation of brain tissue. Proteins of right hemi-forebrains of 5-, 8-, and 12-month-old rT2 and rT3 mice (Table 1) were biochemically isolated as cytosolic and light membrane (Fraction 1), synaptosome (Fraction 2), and PSD (Fraction 3) as described previously (Wang et al., 2013; Gamache et al., 2020). Briefly, tissue specimens were homogenized in buffer 1 (320 mM sucrose; and 25 mM HEPES, pH 7.4) using a Dounce Homogenizer (PolyScience) at the lowest speed for 12 strokes. The resulting homogenates were first centrifuged at 3,000 × g, 4°C for 5 min, and the supernatant was then centrifuged at 10,000 × g, 4°C for 12 min. The resulting supernatant was collected as Fraction 1. The pellet was resuspended in buffer 2 (25 mM HEPES, pH 7.4; 150 mM NaCl; and 2% (v/v) Triton X-100), incubated on ice for 30 min, and then centrifuged at 10,000 × g, 4°C for 20 min. The resulting supernatant was collected as Fraction 2. The pellet was washed once with ice-cold buffer 3 (10 mM sodium phosphate, pH 7.4; 137 mM NaCl; and 2.7 mM KCl) and then resuspended in 250 μl of ice-cold buffer three to obtain Fraction 3.

In vitro *synthesis of Δtau314 protein.* Δtau314 protein was synthesized using previously described methods (Liu et al., 2019). Briefly, cDNA encoding *MAPT* (0N4R isoform) was cloned into the pcDNA3.1(+) vector (Thermo Fisher Scientific). The trinucleotides encoding leucine 315 were modified to a stop codon using the QuikChange II Site-Directed Mutagenesis Kit (Agilent Technologies) following the manufacturer's instructions. The following primers were used for the mutagenesis: forward, 5′-AGTCTACAAACCAGTTGACTAGAGC AAGGTGACCTCCAAG-3′; and reverse, 5′-CTTG GAGGTCACCTTGCTCTAGTCAACTGGTTTGTA GACT-3′. Protein synthesis was conducted using a TnT Coupled Reticulocyte Lysate Systems (Promega) following the manufacturer's instructions.

Immunoprecipitation. Immunoprecipitation was performed according to a previously published protocol (Liu et al., 2019). Briefly, to detect Δtau314, water-soluble brain extracts containing 1.2 mg of total protein per sample were incubated with mouse monoclonal htau antibody tau-13 (BioLegend; 10 μg per reaction; Table 2) and Protein G Sepharose four Fast Flow resin (GE Healthcare) in the presence of protease and phosphatase inhibitors at 4°C for 14-16 h. Resins were then washed in 1× TBS, pH 7.4, with 0.1% (v/v) Triton X-100. The precipitated proteins were eluted at 95°C using 4× loading buffer (Bio-Rad).

Western blotting (WB). WB was performed according to a previously published protocol (Liu et al., 2019). Briefly, protein samples were size-fractionated by SDS-PAGE using 10% Criterion TGX stain-free protein gels (Bio-Rad) and then electrophoretically transferred onto 0.2-μm nitrocellulose membranes at 0.4 A (constant current), 4°C for 4 h.

To compare the expression levels of htau between rT2 and rT3 mice, protein extracts (4 μg per animal) were subjected to WB. Blots were

90 min. The resulting supernatant was depleted of endogenous mouse IgG using Protein G Sepharose 4 FF resin (GE Healthcare) and stored at −80°C until further use.

To compare the expression levels of htau (Table 1; see Fig. 3B), 2-month-old rT2 and rT3 mice were used. The forebrain of the right hemisphere was isolated, and proteins were extracted as described above.

To determine the relative levels of htau to mtau (Table 1; see Fig. 3C), 2-month-old rT2 and rT3 mice and their respective, age-matched transgenic littermates expressing only tTA were used. The forebrain of the right hemisphere was isolated, and proteins were extracted as described above except that phosphatase inhibitor cocktails were excluded.

To determine levels of Δtau314 (Table 1; see Fig. 4), 5- to 9-month-old rT2 and 5- to 9-month-old rT3 mice and their respective 5- to 9-month-old non-transgenic (non-Tg) littermates were used. Water-soluble brain extracts were prepared as previously described (Shankar et al., 2008; Liu et al., 2019). Briefly, the forebrain of the right hemisphere

probed with mouse monoclonal tau-13 antibody (BioLegend; Table 2) or anti-βIII-tubulin (Millipore Sigma; Table 2) at RT for 1 h, followed by HRP-conjugated anti-mouse IgG (Thermo Fisher Scientific).

To determine the relative levels of htau to mtau in rT2 and rT3 mice, protein extracts were subjected to dephosphorylation treatment using calf intestinal alkaline phosphatase (New England Biolabs) as described previously (Gamache et al., 2020). The phosphatase-treated brain proteins (4 µg per animal) were then subjected to WB. Blots were probed with mouse monoclonal T46 antibody (BioLegend; Table 2) or anti-βIII-tubulin (Millipore Sigma; Table 2) at RT for 1 h, followed by HRP-conjugated anti-mouse IgG (Thermo Fisher Scientific).

To determine levels of Δtau314 in rT2 and rT3 mice, eluted tau-13-precipitated proteins were subjected to WB. To reveal Δtau314, blots were probed with mouse monoclonal biotin-conjugated 4F3 (Table 2) at 4°C overnight, followed by HRP-conjugated neutravidin (Thermo Fisher Scientific). To reveal full-length (fl) htau (fl-htau), the same blots were stripped with Restore PLUS stripping buffer (Thermo Fisher Scientific) at RT for 1 h and reprobed with mouse monoclonal biotin-conjugated tau-5 (Thermo Fisher Scientific; Table 2) at RT for 1 h, followed by HRP-conjugated neutravidin (Thermo Fisher Scientific).

To determine levels of fl-htau, phosphorylated tau, and AMPAR in the PSD fraction of rT2 and rT3 mice, homologously resuspended samples (10 µl per animal) were subjected to WB. Total proteins were detected via stain-free imaging technology. Blots were probed with mouse monoclonal antibodies HT7 (Thermo Fisher Scientific; Table 2) and PHF-1 (Table 2) or rabbit polyclonal antibodies (Cell Signaling Technology; Table 2) recognizing AMPAR and PSD95 at RT for 2 h, followed by HRP-conjugated anti-mouse or anti-rabbit IgG (Thermo Fisher Scientific).

WB signals were revealed using either a SuperSignal West Pico PLUS chemiluminescent substrate (Thermo Fisher Scientific) or a highly sensitive Clarity Max Western enhanced chemiluminescence substrate (Bio-Rad) coupled to a semiautomatic ChemiDoc MP Imaging System (Bio-Rad). Image Lab 6.0 (Bio-Rad) was used to perform automatic, unbiased quantification. Experimenters performing WB were blind to mouse genotype, age, and gender.

Simple Western automated WB (SWAWB). SWAWB was performed based on the manufacturer's instructions. Briefly, brain extracts were diluted with 0.1× sample buffer for a final concentration of 18 ng/µl, and then mixed with 5× fluorescent master mix. The resulting samples were denatured by boiling at 95°C for 5 min and then size-fractionated on the ProteinSimple WES System using the 12-230 kDa Separation Module 8 × 25 capillary cartridges (ProteinSimple). Total proteins of the loaded brain extracts were revealed using the total protein detection module. fl-htau proteins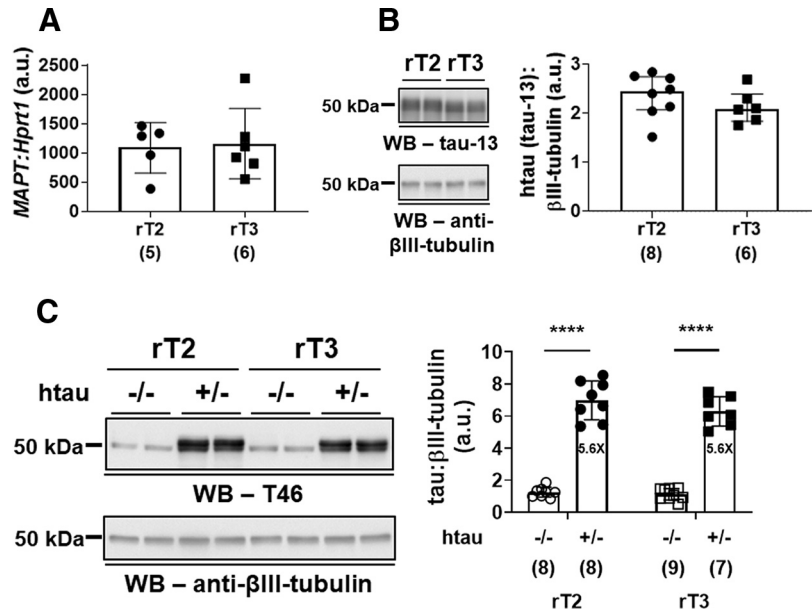 were revealed using mouse monoclonal antibody HT7 (Thermo Fisher Scientific; Table 2) and the anti-mouse detection module.

Immunofluorescence and semiquantitative analyses of tau signals. Following transcardial perfusion with ice-cold 1× PBS (pH 7.4) and decapitation, the left hemisphere was dissected and fixed in 4% (w/v) ice-cold PFA for 48 h. Fixed brain tissue was thoroughly washed with ice-cold 1× PBS (pH 7.4) and then transferred to Antigen Preservative Solution (Neuroscience Associates) for long-term storage at −20°C until further use. Before sectioning, brains were washed thoroughly with ice-cold 1× PBS (pH 7.4) and transferred to 30% (w/v) sucrose (dissolved in 1× PBS, final pH 7.4) to be cryoprotected for 48 h. Brains were then embedded in Tissue-Tek Optimal Cutting Temperature compound (Sakura) and cut into 40-µm-thick coronal sections at −20°C using a Leica CM 1900 cryostat (Leica Microsystems). Brain sections were stored at −20°C in Antigen Preservative Solution until further use.

Figure 3. Quantitative analyses of htau transgene expression in rT2 and rT3 mice. *A*, Quantitative comparison of mRNA levels (normalized to levels of *Hprt1*) of *MAPT* in the forebrain between 2-month-old rT2 and age-matched rT3 mice. The scatter plot with bar graph represents data of individuals plus group mean ± SD. *B*, Quantitative comparison of protein levels (normalized to levels of βIII-tubulin) of fl-htau in the forebrain between 2-month-old rT2 and age-matched rT3 mice. Left, Representative WBs using antibodies recognizing htau (tau-13, top) and βIII-tubulin (bottom). Right, A scatter plot with bar representing individual data plus group median ± interquartile range. *C*, Quantitative comparison of forebrain protein levels (normalized to levels of βIII-tubulin) of dephosphorylated fl-tau (htau plus mtau, +/−) and endogenous fl-mtau (−/−) for 2-month-old rT2 and age-matched rT3 mice. Left, Representative WBs using antibodies recognizing tau (T46, top) and βIII-tubulin (bottom). Right, A scatter plot with bar representing individual data plus group mean ± SD. Numbers of animals (for detailed gender distribution, see Table 1) used are shown in parentheses. ****$p < 0.0001$. a.u., arbitrary units. kDa, kilodaltons.
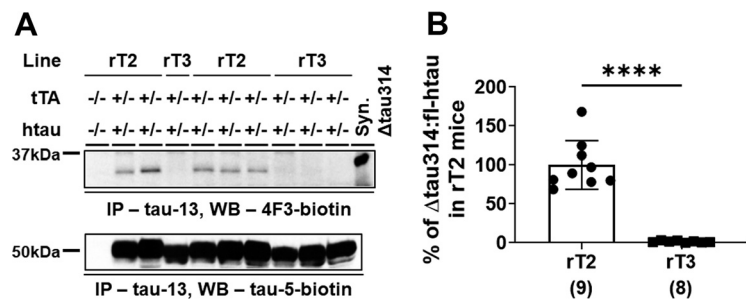

Figure 4. Quantitative comparison of levels of Δtau314 in rT2 and rT3 mice. *A*, Representative Immunoprecipitation (IP)/WBs. Proteins from rT2 and rT3 mice (htau$^{+/−}$ tTA$^{+/−}$) (5- to 9-month-old) captured by tau-13 antibody were revealed using biotin-conjugated 4F3 antibody for the detection of Δtau314 (top). A non-Tg littermate (htau$^{−/−}$ tTA$^{−/−}$) of rT2 mice was used as negative control. Synthetic (Syn.) Δtau314 (6 µl) was used as positive control. fl-htau was detected by reprobing the same blot with biotin-conjugated tau-5 antibody (bottom). *B*, Quantitative comparison of levels of Δtau314 (normalized to levels of fl-htau) in the forebrain between rT2 and rT3 mice. The scatter plot with bar represents individual data plus group mean ± SD. Numbers of animals (for detailed gender distribution, see Table 1) used are shown in parentheses. ****$p < 0.0001$. kDa, kilodaltons.

Table 2. Primary antibodies used in this study

Antibody	Host/isotype	Epitope	Source	Usage[c]
Tau-13	Mouse, IgG$_{1, \kappa}$	tau$_{15-25}$	BioLegend, catalog #835201; RRID:AB_2565341	IP ($\sim$10 µg), WB (1:30,000, final conc.: n.d.)
T46	Mouse, IgG$_1$	tau$_{395-432}$	Thermo Fisher Scientific, catalog #13-6400; RRID:AB_2533025	WB (1:10,000, final conc.: 50 ng/ml)
AT8	Mouse, IgG$_1$	phosphorylated tau at Ser202 & Thr205	Thermo Fisher Scientific, catalog #MN1020; RRID:AB_223647	IF (1:1000, final conc.: 200 ng/ml)
MC1	Mouse, IgG$_1$	conformation-dependent, tau$_{7-9}$ & tau$_{313-322}$	P. Davies gift; RRID:AB_2314773	IF (1:1000, final conc.: n.d.)
CP13	Mouse, IgG$_{2b,}$	phosphorylated tau at Ser202	P. Davies gift; RRID:AB_2314223	IF (1:2000, final conc.: n.d.)
PHF-1	Mouse, IgG$_1$	phosphorylated tau at Ser396 & Ser404	P. Davies gift; RRID:AB_2315150	WB (1:5000, IF (1:1500); final conc.: n.d.
Anti-β III-tubulin	Mouse, IgG$_{2b}$	C-terminus	Millipore Sigma, catalog #T8578; RRID:AB_1841228	WB (1:200,000, final conc.: 5 ng/ml)
Biotin-conjugated 4F3	Mouse, IgG$_{2b, \kappa}$	tau$_{x-314}$	Ashe laboratory	WB (1:45,000, final conc.: 36 ng/ml)
Biotin-conjugated tau-5	Mouse, IgG$_1$	tau$_{210-241}$	Thermo Fisher Scientific, catalog #MA5-12805; RRID:AB_10978000	WB (1:30,000, final conc.: 17 ng/ml)
HT7	Mouse, IgG$_{1, \kappa}$	tau$_{159-163}$	Thermo Fisher Scientific, catalog #MN1000; RRID:AB_2314654	SWAWB (1:100), WB (1:5000), IF (1:10,000, final conc.: 20 ng/ml)
Anti-AMPAR 1 (GluA1)	Rabbit, IgG	proprietary	Cell Signaling Technology, catalog #13185S; RRID:AB_2732897	WB (1:5000, final conc.: n.d.)
Anti-PSD95	Rabbit, IgG	proprietary	Cell Signaling Technology, catalog #2507S; RRID:AB_561221	WB (1:5000, final conc.: n.d.)
Anti-NeuN	Rabbit, IgG	N-terminus	Millipore Sigma, catalog #ABN78; RRID:AB_10807945	IF (1:1000, final conc.: n.d.)

Amino acid residues are counted using the 2N4R human tau splicing isoform numbering system. Ser, Serine; Thr, threonine; conc., concentration; n.d., not determined; IP, immunoprecipitation; IF, immunofluorescence.

To investigate age-related progression of pathologic tau conformation and phosphorylation in neurons of the hippocampus, primary somatosensory cortex (Sm Ctx), and entorhinal cortex (Ent Ctx), three tissue sections were selected for each studied animal. The first section was located at bregma −1.94 mm (interaural 1.86 mm), and subsequent sections were located at bregma −2.42 mm and −2.90 mm, respectively. Tissue plates were placed on gently-rotating orbital shakers during all wash and incubation steps, except for antigen retrieval. Brain sections were first washed 3 times with 1× PBS (pH 7.4) at RT for 5 min each time to rinse off the preservative solution. Next, to reduce autofluorescence, brain sections were incubated in 1% (w/v) sodium borohydride (dissolved in 1× PBS, final pH 9.7) at RT for 20 min. Next, brain sections were washed 5 times with 1× PBS (pH 7.4) at RT for 15 min each time and then incubated in antigen retrieval solution (Reveal Decloaker, RTU, pH 6.0; Biocare Medical) at 80°C for 30 min. Next, brain sections were cooled to RT and then washed with 1× PBS (pH 7.4) 3 times for 5 min each time. Brain sections were then blocked using 5% (v/v) normal goat serum (NGS) (diluting 100% (v/v) NGS solution (Vector Laboratories) in 1× PBS, 0.5% (v/v) Triton X-100, pH 7.4) at RT for 1 h. Next, sections were incubated at 4°C for 48 h in 3% (v/v) NGS (diluting 100% (v/v) NGS solution in 1× PBS, 0.3% (v/v) Triton X-100, pH 7.4) with a rabbit polyclonal antibody recognizing NeuN (Millipore Sigma; Table 2) plus one of the following mouse monoclonal antibodies (Table 2): AT8, CP13, MC1, and PHF-1. After being washed 3 times with 1× PBS (pH 7.4) at RT for 15 min each time, brain sections were incubated in the dark with goat-anti-rabbit IgG-conjugated AlexaFluor-488 (Abcam) (1:1,000, diluted in 3% (v/v) NGS) and goat-anti-mouse IgG-conjugated AlexaFluor-568 (Abcam) (1:1,000, diluted in 3% (v/v) NGS) at RT for 1 h. Following three 15 min washes with 1× PBS (pH 7.4), brain sections were treated with TrueBlack Lipofuscin Autofluorescence Quencher (Biotium) at RT for 30 s, and then washed 3 times with 1× PBS (pH 7.4) for 5 min each time. Finally, brain sections were mounted onto Superfrost Plus charged slides, coverslipped with Vectashield Mounting Medium with DAPI (Vector Laboratories), and stored at 4°C.

Digital immunofluorescence photomicrographs were obtained using a Nikon C2 confocal microscope (Nikon) with a 10× (NA = 0.45) objective located at the UIC. NIS-Elements software (Nikon) was used to drive sequential scanning of ROIs in three fluorescence channels: a DAPI laser (excitation: 405 nm, emission: 460 nm), a GFP laser (excitation: 488 nm, emission: 519 nm), and a Texas Red laser (excitation: 561 nm, emission: 617 nm).

Photomicrographs were acquired as Z stacks (imaged through 40 µm depth) and collapsed into maximum intensity projection images. Following

Table 3. Semiquantitative grading scales of tau pathology

ROI	CA1	CA2-3	DG	Sm Ctx	Ent Ctx
			Counts[a]		
Scale[b]					
0	0	0	0	0	0
0.5	1-2	1-2	1	1-2	1-2
1	3-4	3-4	2	3-4	3-4
1.5	5-9	5-6	3	5-9	5-9
2	10-14	7-8	4	10-14	10-14
2.5	15-19	9-10	5	15-19	15-19
3	≥20	≥11	≥6	≥20	≥20

[a]Counts = the number of immunoreactive neuronal cell bodies identified within a single FOV.
[b]Scale = Semiquantitative unit in the y axes of Figure 8B-E.

collection, images were processed using ImageJ software (National Institutes of Health). Specifically, background was subtracted using the Rolling ball radius (50.0 pixels) function. Large hippocampal images were created using the pairwise stitching plugin.

Tau immunoreactivity at five anatomic ROIs (i.e., cornu ammonis (CA)1, CA2-3, dentate gyrus (DG), primary Sm Ctx, and Ent Ctx) were graded in a semiquantitative manner using adapted Consortium to Establish a Registry for Alzheimer's Disease (AD) neuropsychological rating scales as previously described (Santacruz et al., 2005; Gamache et al., 2019). Immunostained brain sections were viewed, and the quantity of cells containing immunoreactive htau signals was graded through a 10× ocular and a 20× (NA = 0.45) objective equipped to a Zeiss Axioskop 2 MOT fluorescence microscope (Zeiss) under the excitation wavelength of 555 nm. ROIs were exhaustively examined through nonoverlapped FOVs. For each brain section, a score (Table 3) was assigned for each FOV of a specific ROI, and the average score was then calculated for each ROI. The resulting scores of a particular ROI from different brain sections of a mouse were averaged and then used for semiquantitative analysis. The experimenter assigning scores was blind to mouse genotype, age, and gender.

Hippocampal cell volume quantification. Mouse brain processing and sectioning were prepared as described in Immunofluorescence and semiquantitative analyses of tau signals. For each studied mouse, five sections spanning the hippocampus were systematically selected (360 µm apart, coordinates: bregma (mm) −1.42, −1.78, −2.14, −2.50, and −2.86). The selected brain sections were first washed 3 times with 1× PBS (pH 7.4) at RT for 5 min each time to rinse off the preservative solution. Next, brain sections were incubated in 1% (w/v) sodium borohydride at RT for

20 min to reduce autofluorescence. Next, brain sections were washed 5 times with 1× PBS (pH 7.4) at RT for 5 min each time and then incubated in antigen retrieval solution (Reveal Decloaker, RTU) at 80°C for 30 min. Brain sections were cooled to RT and then washed 3 times with 1× PBS (pH 7.4) for 5 min each time. Next, brain sections were blocked using 5% (v/v) NGS at RT for 1 h, followed by incubation at 4°C for 48 h in 3% (v/v) NGS with a rabbit polyclonal antibody recognizing NeuN (Millipore Sigma; Table 2) and mouse monoclonal antibody HT7 (Thermo Fisher Scientific; Table 2). After being washed with 1× PBS (pH 7.4) 3 times at RT for 15 min each time, brain sections were incubated in the dark with goat-anti-rabbit IgG-conjugated AlexaFluor-488 (Abcam) (1:1,000, diluted in 3% (v/v) NGS) and goat-anti-mouse IgG-conjugated AlexaFluor-594 (Abcam) (1:1,000, diluted in 3% (v/v) NGS) at RT for 1 h. Following 3 times of a 15 min wash with 1× PBS (pH 7.4), brain sections were treated with TrueBlack Lipofuscin Autofluorescence Quencher at RT for 30 s, and then washed 3 times with 1× PBS (pH 7.4) for 5 min each time. Finally, brain sections were mounted onto Superfrost Plus charged slides, coverslipped with Vectashield Mounting Medium with DAPI, and stored at 4°C.

Digital immunofluorescence photomicrographs were obtained using a Nikon C2 confocal microscope (Nikon) with a 4× (NA = 0.13) objective located at the UIC. NIS-Elements software (Nikon) was used to drive scanning the entire ROI in three fluorescence channels: DAPI, GFP, and Texas Red.

Hippocampal area measurements were obtained using ImageJ software (National Institutes of Health). The freehand tool was used to measure the area of the pyramidal cell layer (PCL) of the hippocampal regions (CA1, CA2-3) and the granule cell layer (GCL) of the DG in each section. Two experimenters blind to age, gender, and genotype conducted area measurements, and mean values were used for statistical analyses.

Stereology-based estimation of the volume (V) of neuronal cell layers in hippocampus was conducted using the following equation:

$$V = t\Sigma Ai,$$

where t is the distance between two consecutively sampled sections (i.e., 400 μm) and Ai is the measured area of ROI in each studied brain section.

Morris water maze (MWM). Spatial reference memory was assessed using a previously described MWM protocol (Liu et al., 2015b; Gamache et al., 2020) (see Fig. 5A) customized for fast-learning 129S6/FVB F1 mice (Weitzner et al., 2015) to enhance sensitivity to subtle deficits (Westerman et al., 2002). Briefly, prehandling of mice (one session per day for 5 consecutive days) was conducted 1 week before the behavioral test to acclimate animals to the test environment and alleviate stress-induced deficit in performance (Sandi, 1998; Holscher, 1999). Three days following prehandling, mice underwent visible-platform training (three trials per day for 5 consecutive days; intertrial interval: 20-30 min) and then hidden-platform training (two trials per day for 8 d; intertrial interval: 20-30 min). There was a 2 d interval between the last visible, and the first hidden, platform training trial. In each training trial, each mouse was allowed 60 s to locate the platform. The escape latencies of visible training trials within each day were averaged for data analyses. The escape latencies of hidden training trials were averaged over 2 d periods (i.e., combining days 1 and 2, days 3 and 4, days 5 and 6, and days 7 and 8, respectively) for data analyses. Three 30 s probe trials, in which mice were allowed to search for the platform (removed from the pool), were performed 72 h after the eighth, 12th, and 16th trials of hidden-platform training. The first and second probe trials were followed immediately by hidden training. The mean values of quadrant occupancy of the three probe trials were used for statistical analyses. All trials were monitored and recorded using a computerized tracking system (Noldus EthoVision XT 10; Noldus Noldus Information Technology). Experimenters conducting the behavioral test were blind to mouse genotype.

Experimental design and statistical analyses. The experimental design for determining the spatial expression pattern of transgenic human tau expression (both mRNA and protein) is described in detail in mRNA ISH and Protein extraction. As this was a qualitative study, no statistical analysis was applied.

Statistical analyses for all the quantitative data were performed using GraphPad Prism version 8.3.0 (GraphPad Software), except for multiple linear regression analyses of age-related progression of pathologic tau conformation and phosphorylation, which was performed using R version 3.4.1 (R Foundation for Statistical Computing). Data that passed normality tests were subjected to parametric tests, whereas those that did not were subjected to nonparametric tests. $p < 0.05$ was considered statistically significant.

The experimental design for measuring mRNA levels of htau by RT-qPCR is described in detail in RNA extraction, qRT-PCR, and Table 1. The sample sizes (N values) used in this experiment were determined from power analyses of a similar experiment as described previously (Gamache et al., 2020). To assess differences in mRNA levels of htau between rT2 and rT3 mice, an unpaired, two-tailed t test with Welch's correction was used.

For protein levels of tau measured by WB, the experimental design is detailed in Protein extraction, WB, and Table 1. The N values used were determined from power analyses described previously (Gamache et al., 2020). To assess differences in protein levels of htau between rT2 and rT3 mice, an unpaired, two-tailed Mann–Whitney U test was used. To compare protein levels of htau relative to endogenous mtau in rT2 and rT3 mice, two-way ANOVA was used followed by *post hoc* tests between groups (Tukey's multiple comparisons).

For levels of Δtau314 measured by immunoprecipitation/WB, the experimental design is detailed in Protein extraction, Immunoprecipitation, WB, and Table 1. The N values used were determined from power analyses of a preliminary study using a smaller sample size. To assess differences in levels of Δtau314 between rT2 and rT3 mice, an unpaired, two-tailed t test with Welch's correction was used.

For WB-measured levels of fl-htau, phosphorylated tau, and AMPAR in the PSD fraction, the experimental design is detailed in Subcellular fractionation of brain tissue, WB, Figure 9, and Table 1. The N values used were determined from power analyses of a preliminary study using a smaller sample size. To compare fl-htau protein levels between rT2 and rT3 mice within each studied age, an unpaired, two-tailed t test with Welch's correction was used. To compare levels of phosphorylated tau and AMPAR between rT2 and rT3 mice within each studied age, two-way ANOVA was used to study the htau mutation (D314E) × transgene interaction followed by *post hoc* tests (Tukey's multiple comparisons). To assess age-related alteration in protein levels between rT2 and rT3 mice, two-way ANOVA was used to study the htau mutation (D314E) × age interaction followed by *post hoc* tests (Tukey's multiple comparisons), non-Tg littermates of rT2 and rT3 mice were not included in this analysis.

Detailed experimental design and statistical analyses for the behavioral test, including numbers of animals of each gender used for each of the three studied ages (i.e., 5, 8, and 12 months), are described in Morris water maze (MWM), Figure 5, and Table 1. The N values used were determined based on power analyses described previously (Gamache et al., 2020). In order to assess spatial reference learning of rT2 and rT3 mice at each of the three studied ages, two-way repeated-measures ANOVA followed by Sidak's multiple comparisons was used for visible- and hidden-platform trials of MWM to determine whether escape latencies differed between transgenic mice (rT2 or rT3) and their corresponding non-Tg littermates. In order to assess spatial reference memory of rT2 and rT3 mice at each of the three studied ages, the Dirichlet distribution (Maugard et al., 2019) was first used to determine whether mice spent the same percentage of time in each of the four quadrants. *Post hoc* comparisons were then performed using either one-tailed single-sample t tests (for target or opposite quadrant) or two-tailed single-sample t tests (for adjacent quadrants) (Maugard et al., 2019) to assess whether the fractions of time mice spent in each quadrant were different from 25%.

For analyzing volumes of PCL and GCL, experimental design and statistical analyses are described in Hippocampal cell volume quantification, Figure 6, and Table 1. To compare cell layer volumes among mice, two-way ANOVA was used followed by Tukey's multiple comparisons. Specifically, cell layer volumes of non-Tg littermates of rT1, rT2, and rT3 mice at each of the five studied ages (i.e., 5, 8, 12, 15, and 18 months) were first compared. No difference was detected (data not shown); therefore, non-Tg mice of the same age were combined and then compared with transgenic mice.
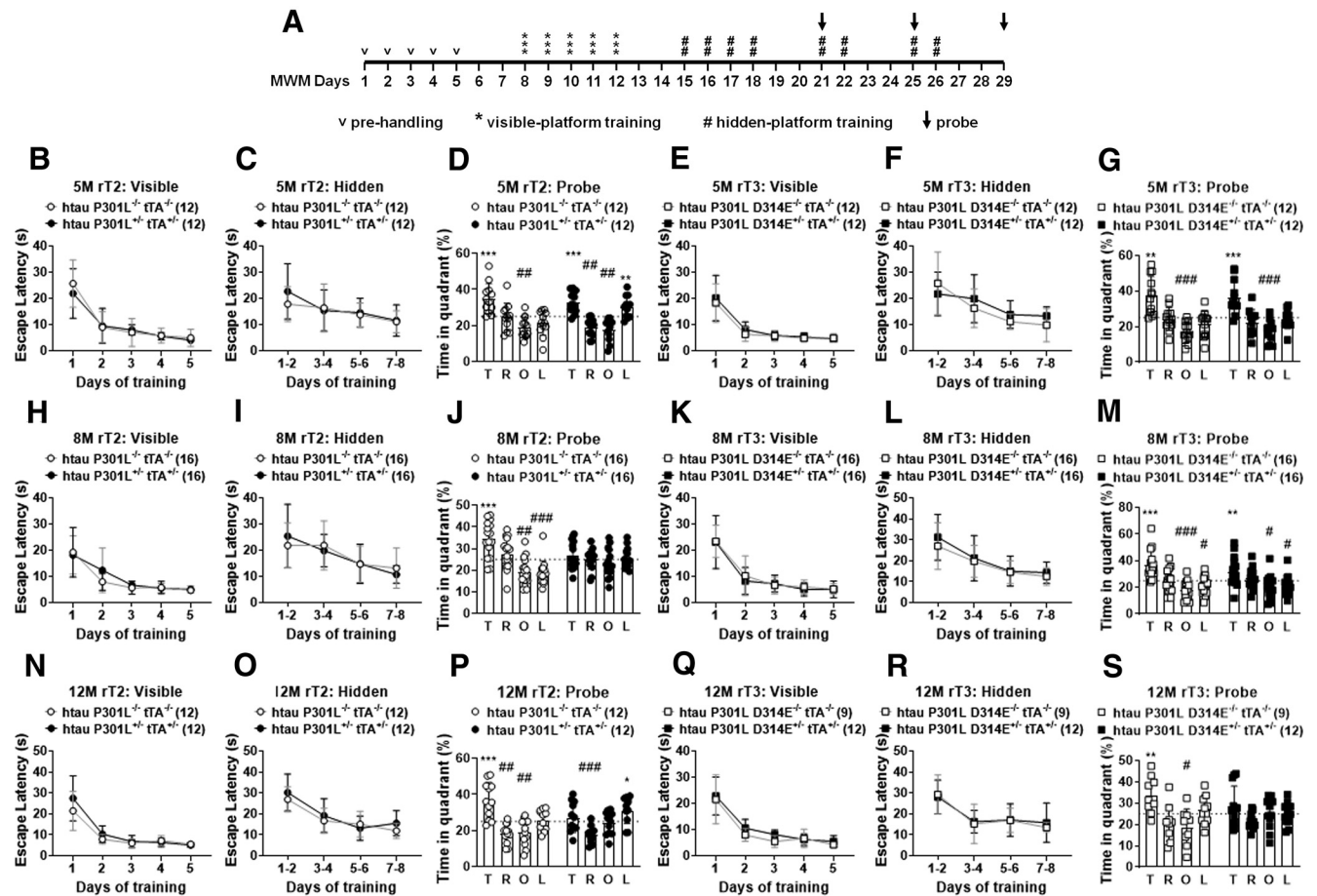
Figure 5. Age-related spatial reference learning and memory in rT2 and rT3 mice. *A*, A schematic diagram illustrating the experimental procedures of MWM used to measure spatial reference learning and memory of rT2 and rT3 mice at 5, 8, and 12 months of age. Detailed description is available in Materials and Methods. *B–S*, Superimposed symbols with bars (group mean ± SD) and connecting line graphs (*B,C,E,F,H,I,K,L,N,O,Q,R*) show data of the visible- and hidden-platform trials. Scatter plot with bar (individual data plus group mean ± SD) graphs (*D,G,J,M,P,S*) show data of the probe phase with the 25% chance level shown in dotted lines. *Post hoc* analyses following the Dirichlet distribution were performed to identify differences between each of the four quadrant occupancies and the chance level. Numbers of animals (for detailed gender distribution, see Table 1) used are shown in parentheses. $*p < 0.05$, $**p < 0.01$, $***p < 0.001$ (for quadrant occupancies $>25\%$). $\#p < 0.05$, $\#\#p < 0.01$, $\#\#\#p < 0.001$ (for quadrant occupancies $<25\%$). T, Target quadrant; R, right quadrant; O, opposite quadrant; L, left quadrant. htau P301L$^{+/-}$ tTA$^{+/-}$, rT2 mice; htau P301L$^{-/-}$ tTA$^{-/-}$, non-Tg littermates of rT2 mice; htau P301L D314E$^{+/-}$ tTA$^{+/-}$, rT3 mice; htau P301L D314E$^{-/-}$ tTA$^{-/-}$, non-Tg littermates of rT3 mice. M, months of age.

For the brain weight analyses, experimental design and statistical analyses are described in the legend of Figure 7 and Table 1. To compare brain weights among mice, two-way ANOVA was used followed by Tukey's multiple comparisons. Specifically, brain weights of non-Tg littermates of rT1, rT2, and rT3 mice at each of the five ages described above were first compared. No difference was detected (data not shown); therefore, non-Tg mice of the same age were combined and then compared with transgenic mice.

For analysis of the age-related progression of pathologic tau conformation and phosphorylation in neuronal cell bodies, experimental design and statistical analyses are described in Immunofluorescence and semiquantitative analyses of tau signals, Figure 8, and Table 1. Multiple linear regression analyses were performed to test for an age-associated progression in tau immunoreactivities and determine whether the rates of age-related progression of tau immunoreactivities differed between rT2 and rT3 mice. As rT1 mice showed no tau immunoreactivity, only data of rT2 and rT3 mice were used for statistical analyses.

All data are openly accessible on request. None of the experiments described in this report has been preregistered.

Results

Transgenic htau expression in rT2 and rT3 mice
To explore the spatial expression pattern of htau transgenes of rT2 and rT3 mice, we showed that *MAPT* mRNA was detected

in the cerebral cortex, hippocampus, caudate putamen, and olfactory bulb, but not the brainstem or cerebellum in 2-month-old animals (Fig. 2A). In parallel, we showed that htau proteins were detected in the cerebral cortex, hippocampus, and olfactory bulb, but not the brainstem, cerebellum, or spinal cord in mice of the same age (Fig. 2B). These findings confirm a forebrain-specific htau transgene expression driven by *CaMKIIα* promoter.

To compare the forebrain expression levels of htau transgenes in rT2 and rT3 mice, we quantified levels of *MAPT* mRNA and observed no difference ($t_{(8.869)} = 0.2322$, $p = 0.8217$) between the two transgenic lines at 2 months of age (Fig. 3A). Using WB probed with tau-13 antibody, we showed that levels of fl-htau proteins were comparable ($U = 15$, $p = 0.2824$) in the forebrain between rT2 and rT3 mice at 2 months of age (Fig. 3B). In addition, we observed a transgene-dependent alteration ($F_{(1,28)} = 388.7$, $p < 0.0001$) in levels of dephosphorylated fl-tau proteins. *Post hoc* analysis showed that levels of dephosphorylated fl-tau proteins (htau plus mtau) in both rT2 and rT3 mice were 5.6-fold higher ($p < 0.0001$) than levels of dephosphorylated endogenous fl-mtau proteins in their respective littermates expressing only the activator transgene (Fig. 3C). This is consistent with previous
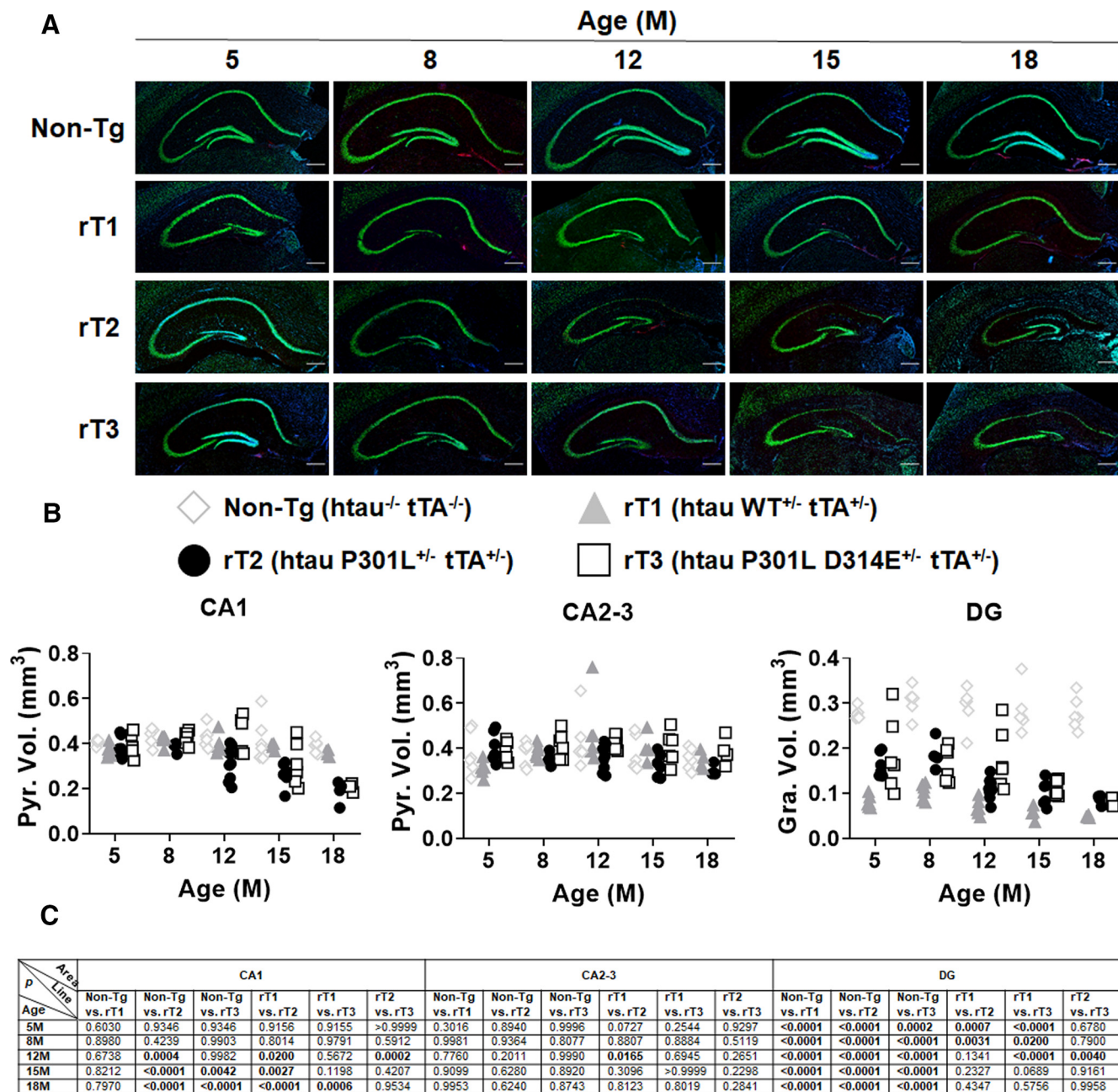
Figure 6. Hippocampal PCL and GCL volume in rT1, rT2, and rT3 mice. *A,* Representative photomicrographs of hippocampi (bregma: −2.18 mm) at varied ages of rT1, rT2, rT3, and non-Tg (combining non-Tg littermates of rT1, rT2, and rT3 mice at the same age; for details, see Experimental design and statistical analyses) mice. Scale bars, 300 μm. *B,* Scatterplots illustrating the volumes of PCLs of the CA1 (left) and CA2-3 (middle), and GCL of the DG (right). Pyr. Vol., PCL volume; Gra. Vol., GCL volume. *C,* Post hoc comparisons of cell layer volumes at varied ages between mouse lines. *p* values of <0.05 are highlighted in bold. M, months of age. For detailed gender distribution and numbers of animals used, see Table 1.

	CA1						CA2-3						DG					
p / Age	Non-Tg vs. rT1	Non-Tg vs. rT2	Non-Tg vs. rT3	rT1 vs. rT2	rT1 vs. rT3	rT2 vs. rT3	Non-Tg vs. rT1	Non-Tg vs. rT2	Non-Tg vs. rT3	rT1 vs. rT2	rT1 vs. rT3	rT2 vs. rT3	Non-Tg vs. rT1	Non-Tg vs. rT2	Non-Tg vs. rT3	rT1 vs. rT2	rT1 vs. rT3	rT2 vs. rT3
5M	0.6030	0.9346	0.9346	0.9156	0.9155	>0.9999	0.3016	0.8940	0.9996	0.0727	0.2544	0.9297	<0.0001	<0.0001	0.0002	0.0007	<0.0001	0.6780
8M	0.8980	0.4239	0.9903	0.8014	0.9791	0.5912	0.9981	0.9364	0.8077	0.8807	0.8884	0.5119	<0.0001	<0.0001	<0.0001	0.0031	0.0200	0.7900
12M	0.6738	0.0004	0.9982	0.0200	0.5672	0.0002	0.7760	0.2011	0.9990	0.0165	0.6945	0.2651	<0.0001	<0.0001	<0.0001	0.1341	<0.0001	0.0040
15M	0.8212	<0.0001	0.0042	0.0027	0.1198	0.4207	0.9099	0.6280	0.8920	0.3096	>0.9999	0.2298	<0.0001	<0.0001	<0.0001	0.2327	0.0689	0.9161
18M	0.7970	<0.0001	<0.0001	<0.0001	0.0006	0.9534	0.9953	0.6240	0.8743	0.8123	0.8019	0.2841	<0.0001	<0.0001	<0.0001	0.4347	0.5756	0.9958

findings (Gamache et al., 2020). Together, these results suggest a comparable level of htau transgene overexpression between rT2 and rT3 mice.

The production of Δtau314 in rT2 and rT3 mice
The D314E mutation was shown to block the production of Δtau314 *in vitro* and in mice expressing htau P301L previously (Zhao et al., 2016). To further determine the effect of this mutation on site-specific cleavage at D314, we compared levels of Δtau314 in age-matched, young rT2 and rT3 mice (Fig. 4*A*,*B*). We showed that levels of Δtau314 were reduced ($t_{(8.024)}$ = 9.502, $p < 0.0001$) by 98.6% in rT3 compared with

rT2 mice, suggesting that the D314E mutation prevents Δtau314 production in transgene targeted-insertion mice constitutively expressing htau P301L.

Spatial memory impairment is delayed in rT3 mice compared with rT2 mice
In rTg4510 mice, lowering levels of murine Casp2 is associated with a reduced production of Δtau314 and reversal of spatial memory impairment (Zhao et al., 2016). In addition, transfection of mice with AAV carrying the Casp2 cleavage-resistant D314E mutation of htau P301L prevents htau transgene-induced cognitive deficits (Zhao et al., 2016). Because of limitations of those
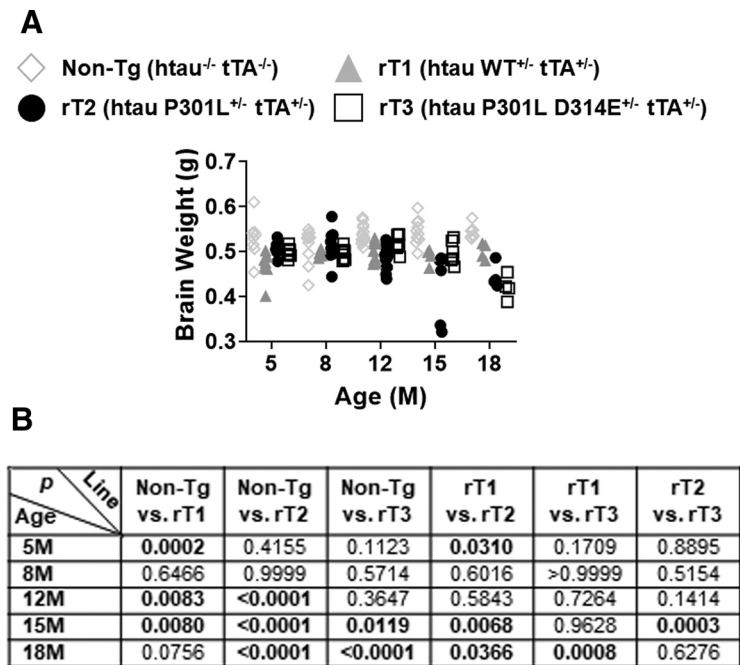
A

B

p \ Line / Age	Non-Tg vs. rT1	Non-Tg vs. rT2	Non-Tg vs. rT3	rT1 vs. rT2	rT1 vs. rT3	rT2 vs. rT3
5M	**0.0002**	0.4155	0.1123	**0.0310**	0.1709	0.8895
8M	0.6466	0.9999	0.5714	0.6016	>0.9999	0.5154
12M	**0.0083**	**<0.0001**	0.3647	0.5843	0.7264	0.1414
15M	**0.0080**	**<0.0001**	**0.0119**	**0.0068**	0.9628	**0.0003**
18M	0.0756	**<0.0001**	**<0.0001**	**0.0366**	**0.0008**	0.6276

Figure 7. Brain weights of rT1, rT2, and rT3 mice. **A**, A scatterplot illustrating the wet brain weights of rT1, rT2, rT3, and non-Tg (combining non-Tg littermates of rT1, rT2, and rT3 mice at the same age; for details, see Experimental design and statistical analyses) mice. **B**, Post hoc comparisons of brain weights at varied ages between mouse lines. p values of <0.05 are highlighted in bold. M, months of age. For detailed gender distribution and numbers of animals used, see Table 1.

two experimental systems, we assessed age-related spatial reference learning and memory in rT2 and rT3 mice via a customized MWM paradigm (Fig. 5A) to better understand the role of the site-specific htau cleavage in cognitive function.

We found no difference in escape latency (Fig. 5B,C,E,F,H,I,K,L,N,O,Q,R) or swimming speed (data not shown) of rT2 or rT3 mice at 5, 8, or 12 months of age compared with their respective, age-matched non-Tg littermates for either visible- or hidden-platform training. These findings indicate normal motor function and task-learning capability of these htau-transgenic mice.

We then analyzed quadrant occupancy of the probe phase using the Dirichlet distribution (Maugard et al., 2019), as the data lack the normal distribution and independence required in performing parametric statistics. We first asked whether mice spent different amounts of time searching (i.e., occupancy) in the four quadrants. At 5 months of age, similar to their respective non-Tg littermates, rT2 (Fig. 5D) as well as rT3 (Fig. 5G) mice spent different amounts of time among the quadrants ($P_{Dirichlet}$ < 0.0001 for both rT2 mice and their non-Tg littermates, and $P_{Dirichlet}$ = 0.0004 and 0.0016 for rT3 mice and their non-Tg littermates, respectively). We then asked how occupancies in each of the four quadrants differ from chance. We found occupancies significantly higher than 25% for the target quadrant and lower than 25% for the opposite quadrant in both rT2 and rT3 mice as well as their respective non-Tg littermates (Fig. 5D, G), indicating normal memory function in 5-month-old animals (target occupancy for mice: rT2: $t_{(11)}$ = 4.6509, p = 0.0004; rT3: $t_{(11)}$ = 4.1493, p = 0.0008; non-Tg rT2 littermates: $t_{(11)}$ = 4.0949, p = 0.0009; and non-Tg rT3 littermates: $t_{(11)}$ = 4.0100, p = 0.0010; opposite-target occupancy for mice: rT2: $t_{(11)}$ = −4.0111, p = 0.0010; rT3: $t_{(11)}$ = −4.3041, p = 0.0006; non-Tg rT2

littermates: $t_{(11)}$ = −3.6501, p = 0.0019; and non-Tg rT3 littermates, $t_{(11)}$ = −4.9844, p = 0.0002).

At 8 months of age, however, we found that rT2 mice occupied the quadrants for similar amounts of time (Fig. 5J), but occupancies remained different in rT3 mice (Fig. 5M), in non-Tg rT2 littermates (Fig. 5J), and in non-Tg rT3 littermates (Fig. 5M) ($P_{Dirichlet}$ = 0.44 for rT2 mice, $P_{Dirichlet}$ = 0.0059 for rT3 mice, and $P_{Dirichlet}$ < 0.0001 for their respective non-Tg littermates). Post hoc analyses showed no quadrant occupancy difference from 25% for rT2 mice but significantly higher than 25% for the target quadrant and lower than 25% for the opposite quadrant for rT3 mice as well as their respective non-Tg littermates (target occupancy for mice: rT3: $t_{(15)}$ = 2.6026, p = 0.0100; non-Tg rT2 littermates: $t_{(15)}$ = 4.5857, p = 0.0002; and non-Tg rT3 littermates, $t_{(15)}$ = 4.6748, p = 0.0002; opposite-target occupancy for mice: rT3: $t_{(15)}$ = −2.1160, p = 0.0257; non-Tg rT2 littermates: $t_{(15)}$ = −3.7132, p = 0.0010; and non-Tg rT3 littermates: $t_{(15)}$ = −4.4220, p = 0.0002) (Fig. 5J, M). These results indicate that memory function is impaired in rT2 mice but remains normal in rT3 mice.

At 12 months of age, we found that occupancies in the four quadrants were no longer different in rT3 mice (Fig. 5S) ($P_{Dirichlet}$ = 0.31 and 0.011 for rT3 mice and their non-Tg littermates, respectively). Post hoc analyses showed no quadrant occupancy difference from 25% for rT3 mice (Fig. 5S), indicating their impaired memory function. Although significantly different quadrant occupancies were observed in 12-month-old rT2 mice (Fig. 5P) ($P_{Dirichlet}$ = 0.0012 and < 0.0001 for rT2 mice and their non-Tg littermates, respectively), this was driven mainly by markedly high and low occupancies of adjacent quadrants rather than those of the target and opposite quadrants, which showed no difference from 25% (Fig. 5P). These results indicate that memory function of 12-month-old rT2 mice remains impaired.

Together, these findings suggest that expressing the cleavage-resistant D314E mutant in mice delays the onset of, but fails to prevent, htau P301L-induced spatial reference memory impairment. Spatial reference acquisition of mice seems unaffected by this mutant.

Hippocampal neurodegeneration is delayed in rT3 mice compared with rT2 mice

Previous reports indicate that htau cleavage at D314 is required for htau P301L-induced hippocampal volume reduction in young WT mice (Zhao et al., 2016). To better understand the contribution of this cleavage to neurodegeneration, we quantitatively compared volumes of hippocampal PCL and GCL between rT2 and rT3 mice. Here, we also included rT1 mice expressing WT htau (Gamache et al., 2020) to discern the effects of the FTD-linked htau P301L variant from those caused solely by htau expression.

In the CA1, we observed a transgene-dependent, age-related reduction in the PCL volume (transgene effect: $F_{(3,93)}$ = 21.36, p < 0.0001; age effect: $F_{(4,93)}$ = 18.50, p < 0.0001; and transgene × age interaction: $F_{(12,93)}$ = 4.084, p < 0.0001) (Fig. 6A,B). By post hoc analyses, we detected a volume reduction in
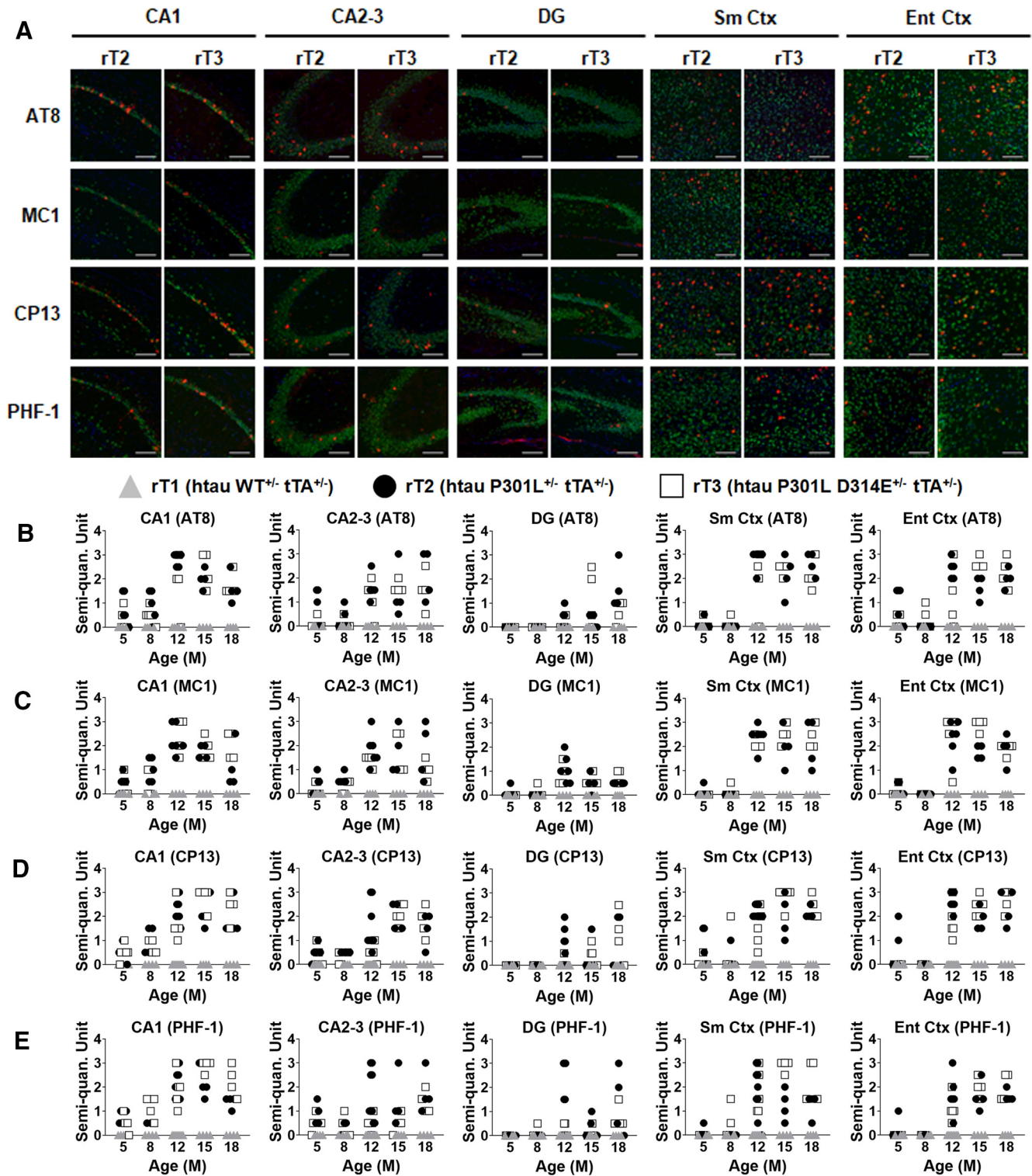
Figure 8. Age-related progression of pathologic tau conformation and phosphorylation in neuronal cells of rT1, rT2, and rT3 mice. *A*, Representative photomicrographs of phosphorylated tau (red punctates) immunoreactive to the antibodies AT8, CP13, or PHF-1, and conformationally altered tau (red punctates) immunoreactive to the antibody MC1 in neuronal cells (NeuN staining in green) of the hippocampus (including CA1, CA2-3, and DG), primary Sm Ctx, and Ent Ctx of 18-month-old rT2 and rT3 mice. Scale bars, 100 μm. *B-E*, Scatterplots illustrating levels of tau reactive to antibodies AT8 (*B*), MC1 (*C*), CP13 (*D*), and PHF-1 (*E*) in the five anatomic brain regions (i.e., CA1, CA2-3, DG, Sm Ctx, and Ent Ctx) of rT1, rT2, and rT3 mice at varied ages. Semi-quan., Semiquantitative. M, months of age. For detailed gender distribution and numbers of animals used, see Table 1.

rT2 mice starting at 12 months of age compared with age-matched non-Tg (lower by 27%, 33%, and 50% at 12, 15, and 18 months, respectively) and rT1 (lower by 21%, 32%, and 49% at 12, 15, and 18 months, respectively) mice (Fig. 6A–C). In addition, no difference in the PCL volume was present between rT1 and non-Tg

mice (Fig. 6A–C). Given a twofold higher htau expression level in rT1 than in genetically matched rT2 mice (Gamache et al., 2020), these results indicate an age-related CA1 neurodegeneration induced by the FTD-linked htau P301L expression. Meanwhile, we found that the CA1 PCL volumes of rT3 mice were lower than

those of non-Tg mice at 15 (by 21%) and 18 (by 45%) months of age and lower than those of rT1 mice at 18 months of age (by 42%); in particular, only the CA1 PCL volumes of 12-month-old rT3 and rT2 mice differed (the former higher by 39%) (Fig. 6A–C). Together, these results indicate that age-related CA1 neurodegeneration is delayed in middle-aged rT3 mice compared with age-matched rT2 mice.

In the CA2-3, although we observed a transgene-induced reduction in the PCL volume ($F_{(3,93)} = 2.781$, $p = 0.0453$), we detected no difference between mouse lines at any test age (Fig. 6A–C, except for 12-month-old rT1 versus rT2 mice, likely because of an rT1 outlier), indicating that CA2-3 neurons are preserved independently of age, transgene expression, and site-specific htau cleavage.

In the DG, we observed a transgene-induced, age-related reduction in the GCL volume (transgene effect: $F_{(3,93)} = 182.6$, $p < 0.0001$; age effect: $F_{(4,93)} = 11.58$, $p < 0.0001$; and transgene × age interaction: $F_{(12,93)} = 2.236$, $p = 0.0158$) (Fig. 6A,B). The presence of lower GCL volumes in the three transgenic htau mouse lines (i.e., rT1, rT2, and rT3) than age-matched non-Tg mice (Fig. 6A–C) is not unexpected as multiple lines of *CKtTA/transgene* bigenic mice modeling various tauopathies consistently exhibit progressive DG neurodegeneration (Jankowsky et al., 2005; Santacruz et al., 2005; Paulson et al., 2008; Han et al., 2012; Liu et al., 2015a; Gamache et al., 2019). Meanwhile, expressing the tTA activator alone has been shown to partially contribute to progressive DG neurodegeneration in mice of certain genetic backgrounds (Han et al., 2012), likely because of tTA-driven off-target gene expression (Gamache et al., 2019). Interestingly, the GCL volumes of young and middle-aged rT1 mice were lower than age-matched rT2 (by 51% and 44% at 5 and 8 months, respectively) and rT3 (by 57%, 37%, and 61% at 5, 8, and 12 months, respectively) mice (Fig. 6A–C). This is likely a consequence of a more severe dysregulation of neurogenesis during the early developmental stage. Specifically, a higher expression level and hyperphosphorylation state of htau in rT1 (than in rT2 and rT3) cause strong detrimental effects (e.g., oxidative stress) during development (Gamache et al., 2020; present study). The GCL volumes of rT2 and rT3 mice became comparable to those of rT1 mice at 12 and 15 months of age, respectively (Fig. 6A–C), likely because of stronger neurodegeneration induced by constitutive expression of FTD-linked htau P301L. Notably, the GCL volumes of rT3 were higher (by 60%) than rT2 mice at 12 months of age but became comparable to rT2 mice starting at 15 months of age (Fig. 6A–C), which indicates a delayed effect of rT3 mice on DG neurodegeneration.

Brain atrophy is delayed in rT3 mice compared with rT2 mice

Age-dependent brain atrophy occurs in htau P301L-expressing rTg4510 and rT2/T2 homozygous mice (Santacruz et al., 2005; Gamache et al., 2019). Since we found delayed hippocampal neurodegeneration in rT3 compared with rT2 mice, we compared brain weights in rT2 and rT3 mice. We observed a transgene-induced, age-dependent brain weight loss (transgene effect: $F_{(3,143)} = 33.81$, $p < 0.0001$; age effect: $F_{(4,143)} = 5.297$, $p = 0.0005$; and transgene × age interaction: $F_{(12,143)} = 6.626$, $p < 0.0001$) (Fig. 7A). When examining mice expressing different htau forms, we detected a reduction in brain weights in rT2 mice (compared with age-matched rT1 mice) by 13% and 11% at 15 and 18 months, respectively (Fig. 7A,B). This was observed despite a

twofold higher htau expression level in rT1 than in rT2 mice (Gamache et al., 2020), indicative of an age-related brain atrophy driven by FTD-linked htau P301L expression. At 15 months of age, rT3 mice had brain weights comparable to rT1 mice but higher than rT2 mice by 16%, whereas brain weights of 18-month-old rT3 mice became comparable to age-matched rT2 mice (Fig. 7A,B), suggesting a delayed brain atrophy effect of rT3 mice relative to rT2 mice.

Age-related progression of pathologic tau conformation and phosphorylation does not differ between rT2 and rT3 mice

Expression of htau P301L in various FTD mouse models leads to an age-related somatodendritic accumulation of hyperphosphorylated and conformationally altered tau forms (Lewis et al., 2000; Ramsden et al., 2005; Terwel et al., 2005; de Calignon et al., 2012; Cook et al., 2015). These effects are similarly observed in the brain of FTD patients (Kovacs, 2015). The abnormal aggregation of these modified tau forms is believed to initiate the formation of neurofibrillary tangles (Ballatore et al., 2007; Bodea et al., 2016), a cardinal brain lesion widely present in neurodegenerative disorders (Kovacs, 2017). To explore the effects of site-specific htau cleavage at D314 on age-related progression of tau pathology, we measured the degree of cell body accumulation of phosphorylated and conformationally altered tau forms in the hippocampus (including CA1, CA2-3, and DG), primary Sm Ctx, and Ent Ctx of rT1, rT2, and rT3 mice (Fig. 8). In mice between 5 and 18 months of age, we observed differences in rates of pathologic tau progression among the three htau-expressing mouse lines (AT8 at CA1, $F_{(2,61)} = 6.413$, $p = 0.0030$; AT8 at CA2-3, $F_{(2,61)} = 7.474$, $p = 0.0012$; AT8 at DG, $F_{(2,61)} = 5.754$, $p = 0.0051$; AT8 at Sm Ctx, $F_{(2,61)} = 17.51$, $p < 0.0001$; AT8 at Ent Ctx, $F_{(2,61)} = 11.39$, $p < 0.0001$; MC1 at CA1, $F_{(2,62)} = 8.217$, $p = 0.0007$; MC1 at CA2-3, $F_{(2,62)} = 7.362$, $p = 0.0014$; MC1 at DG, $F_{(2,62)} = 4.785$, $p = 0.0117$; MC1 at Sm Ctx, $F_{(2,62)} = 22.35$, $p < 0.0001$; MC1 at Ent Ctx, $F_{(2,62)} = 13.46$, $p < 0.0001$; CP13 at CA1, $F_{(2,68)} = 15.12$, $p < 0.0001$; CP13 at CA2-3, $F_{(2,68)} = 8.685$, $p = 0.0004$; CP13 at DG, $F_{(2,62)} = 3.814$, $p = 0.0274$; CP13 at Sm Ctx, $F_{(2,68)} = 17.77$, $p < 0.0001$; CP13 at Ent Ctx, $F_{(2,62)} = 20.22$, $p < 0.0001$; PHF-1 at CA1, $F_{(2,63)} = 9.478$, $p = 0.0003$; PHF-1 at CA2-3, $F_{(2,64)} = 2.198$, $p = 0.1193$; PHF-1 at DG, $F_{(2,60)} = 2.279$, $p = 0.1111$; PHF-1 at Sm Ctx, $F_{(2,63)} = 10.45$, $p = 0.0001$; and PHF-1 at Ent Ctx, $F_{(2,60)} = 18.56$, $p < 0.0001$). We detected no phosphorylated or conformationally altered tau in rT1 mice and no difference in progression rate of AT8-, MC1-, CP13-, or PHF-1-reactive tau signals between rT2 and rT3 mice. These findings indicate that age-related progression of tau pathology is induced by FTD-linked htau P301L as opposed to the WT form, and that site-specific htau cleavage at D314 does not affect the progression of tau pathology.

Age-related postsynaptic abnormalities in rT2 and rT3 mice

Previous research indicates that spatial memory and synaptic plasticity deficits in FTD-modeling mice are associated with excessive accumulation of htau in PSD before synaptic or neuronal loss (Hoover et al., 2010). Furthermore, site-specific htau cleavage at D314 drives htau P301L-induced synaptic dysfunction and cognitive impairment and promotes htau accumulation to dendritic spines in an FTD cellular model (Zhao et al., 2016). To understand the effects of the D314E mutation on tau postsynaptic accumulation *in vivo*, we compared levels of fl-htau (Fig. 9A–E) in rT2 and rT3 mice at 5, 8, and 12 months when their spatial learning and memory were examined. While no difference was detected between rT2 and rT3 mice at 5 (Fig. 9B) or 12
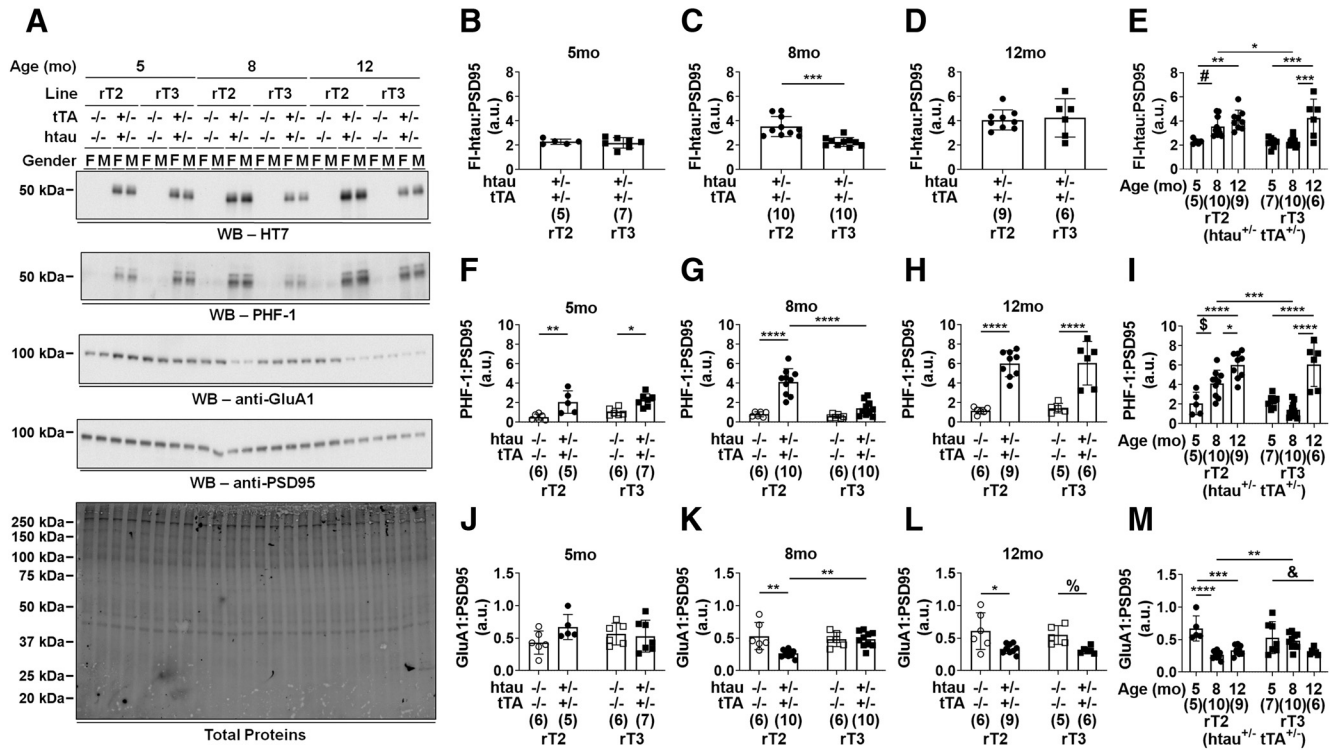
Figure 9. Age-related tau accumulation and AMPAR alteration in PSD of rT2 and rT3 mice. ***A***, Representative WBs showing fl-htau (HT7), phosphorylated tau (PHF-1), GluA1 subunit of AMPAR (anti-GluA1), and PSD95 from a female (F) and a male (M) rT2 and rT3 mice (htau$^{+/-}$ tTA$^{+/-}$) at 5, 8, and 12 months of age (mo) and their respective, age- and gender-matched non-Tg littermates (htau$^{-/-}$ tTA$^{-/-}$). Total PSD proteins were also shown to demonstrate equal loading of samples. kDa, kilodaltons. ***B-M***, Scatter plots with bar (individual data plus group mean ± SD) graphs showing levels of fl-htau (***B-E***), PHF-1-reactive phosphorylated tau (***F-I***), and GluA1 (***J-M***), all normalized to levels of PSD95, in rT2 and rT3 mice at 5 (***B,F,J***), 8 (***C,G,K***), and 12 (***D,H,L***) mo. Age-related alterations between rT2 and rT3 mice (***E,I,M***) were also analyzed. Numbers of animals (for detailed gender distribution, see Table 1) used are shown in parentheses. *$p < 0.05$, **$p < 0.01$, ***$p < 0.001$, ****$p < 0.0001$, $^{\#}p = 0.0715$, $^{\$}p = 0.0576$, $^{\%}p = 0.0895$, $^{\&}p = 0.0525$. a.u., arbitrary units.

(Fig. 9D) months of age, PSD levels of fl-htau were lower ($t_{(12.40)} = 4.465$, $p = 0.0007$) by 36% in rT3 than in rT2 mice at 8 months of age (Fig. 9C). We also observed that this D314E mutation affected htau P301L accumulation in PSD differently at various ages (mutation effect: $F_{(1,41)} = 2.728$, $p = 0.1062$; age effect: $F_{(2,41)} = 19.88$, $p < 0.0001$; and mutation × age interaction: $F_{(2,41)} = 3.886$, $p = 0.0285$) (Fig. 9E). By *post hoc* analyses, we observed that age-related htau P301L accumulation in PSD occurred in both rT2 and rT3 mice, and that the D314E mutation lowered levels of PSD htau P301L specifically in 8-month-old mice. This indicates a delayed effect for the D314E mutation on tau PSD accumulation.

In cultured primary neurons, phosphorylation at serine-396/404 of tau is required to induce its excessive accumulation in dendritic spines (Teravskis et al., 2021), and this early pathologic process disrupts synaptic function (Teravskis et al., 2020). In rT2 and rT3 mice, we investigated whether tau phosphorylated at serine-396/404 (pSer396/404-tau) was excessively accumulated in PSD and whether the D314E mutation alters its PSD presence in an age-dependent manner (Fig. 9A,F–I). We observed a transgene-induced PSD accumulation of pSer396/404-tau in 5-month-old (Fig. 9F) and 12-month-old (Fig. 9H) mice (for the 5-month-old, transgene effect: $F_{(1,20)} = 24.20$, $p < 0.0001$; for the 12-month-old, transgene effect: $F_{(1,22)} = 74.72$, $p < 0.0001$). Compared with levels of pSer396/404-tau in their respective, age-matched non-Tg littermates, levels of pSer396/404-tau were elevated by 3.9-fold ($p = 0.0066$), 2.1-fold ($p = 0.0212$), 5.1-fold ($p < 0.0001$), and 4.2-fold ($p < 0.0001$) in 5-month-old rT2, 5-

month-old rT3, 12-month-old rT2, and 12-month-old rT3 mice, respectively. Notably, we showed that the transgene-induced PSD accumulation of pSer396/404-tau was reversed by the D314E mutation in 8-month-old mice (Fig. 9G) (transgene effect: $F_{(1,28)} = 40.72$, $p < 0.0001$; mutation effect: $F_{(1,28)} = 20.46$, $p = 0.0001$; and transgene × mutation interaction: $F_{(1,28)} = 15.08$, $p = 0.0006$). *Post hoc* analyses showed that levels of pSer396/404-tau were elevated ($p < 0.0001$) by 5.1-fold in rT2 mice compared with their non-Tg littermates and were lower ($p < 0.0001$) by 66% in rT3 compared with rT2 mice. In addition, the D314E mutation age-dependently affects PSD accumulation of pSer396/404-tau (mutation effect: $F_{(1,41)} = 4.484$, $p = 0.0403$; age effect: $F_{(2,41)} = 36.47$, $p < 0.0001$; and mutation × age interaction: $F_{(2,41)} = 6.870$, $p = 0.0027$) (Fig. 9I). *Post hoc* analyses revealed that age-related PSD accumulation of pSer396/404-tau occurred in both rT2 and rT3 mice, and that the D314E mutation lowered PSD levels of pSer396/404-tau specifically in 8-month-old mice.

Excessive postsynaptic tau accumulation is associated with a loss of AMPAR in the membrane of dendritic spines and a reduced strength of AMPAR-mediated synaptic transmission (Hoover et al., 2010). In addition, expression of htau P301L has been shown to reduce levels of AMPAR in PSD in cultured primary neurons, which is reversed by expressing htau P301L D314E (Zhao et al., 2016). To further understand how the D314E mutation affects the PSD anchoring of AMPAR *in vivo*, we compared levels of AMPAR subunit GluA1 (Fig. 9A,J–M) in rT2 and rT3 mice. We observed a transgene-dependent

reduction in levels of GluA1 in 12-month-old mice (Fig. 9L) ($F_{(1,22)}$ = 16.29, $p = 0.0006$). Compared with levels of GluA1 in their respective, age-matched non-Tg littermates, levels of GluA1 were reduced by 45% ($p = 0.0164$) and 43% ($p = 0.0895$) in rT2 and rT3 mice, respectively. Interestingly, the transgene-dependent reduction in levels of GluA1 was prevented by the D314E mutation in 8-month-old mice (Fig. 9K) (transgene effect: $F_{(1,28)}$ = 8.525, $p = 0.0068$; mutation effect: $F_{(1,28)}$ = 3.386, $p = 0.0764$; and transgene × mutation interaction: $F_{(1,28)}$ = 8.711, $p = 0.0063$). Levels of GluA1 were reduced ($p = 0.0015$) by 50% in rT2 mice compared with their non-Tg littermates, but were elevated ($p = 0.0028$) by 1.3-fold in rT3 mice compared with rT2 mice. Further, the D314E mutation affects PSD levels of GluA1 in an age-dependent manner (mutation effect: $F_{(1,41)}$ = 0.1932, $p = 0.6626$; age effect: $F_{(2,41)}$ = 15.84, $p < 0.0001$; and mutation × age interaction: $F_{(2,41)}$ = 7.588, $p = 0.0016$) (Fig. 9M). By *post hoc* analyses, an age-related reduction in PSD levels of GluA1 was detected in rT2 mice, and the D314E mutation preserved PSD levels of GluA1 specifically in 8-month-old mice.

Discussion

In this study, we aimed to better understand the role of a site-specific htau cleavage at D314 in the pathogenesis of FTD. This was achieved by directly comparing progressively aged molecular, pathologic, and behavioral phenotypes in two targeted-insertion mouse lines, rT2 and rT3, which differ only by a cleavage-resistant D314E mutation. Our model system has several advantages. First, htau transgenes are engineered to a genome locus that supports high transgene expression (McCreath et al., 2000). This results in a life-long constitutive htau expression as opposed to the transient htau expression modeled in AAV-transfected mice. This model system also avoids disruption of host functional gene expression as opposed to transgene insertion/deletion (TgINDEL) mutations generated by transgene random insertion (Gamache et al., 2019; Goodwin et al., 2019). Second, the integration of a single copy of htau transgenes in the responder lines results in comparable htau protein levels in rT2 and rT3 mice, which avoids confounding effects associated with inequivalent htau expression in AAV-transfected mice (Zhao et al., 2016). Third, the use of a "tet-off" bigenic system driven by *CaMKIIα* promoter allows htau to be specifically expressed in forebrain neuronal cells. Together, the rT2/rT3 pair serves as an excellent tool to study the effects of the site-specific htau cleavage on multifaceted phenotypes of FTD throughout the lifespan. Notable drawbacks of our bigenic system in disease modeling include the presence of TgINDEL mutations in the activator CaMKIIα-tTA line (Gamache et al., 2019; Goodwin et al., 2019) and the non-physiological overexpression of htau transgene. In particular, the undefined contribution of the tTA TgINDEL allele to mouse phenotypes prevents us from delineating the pathologic effects induced solely by the FTD-linked htau P301L variant. However, as the same TgINDEL allele was used to drive htau expression in both rT2 and rT3 mice, the tTA TgINDEL-associated confounding effects are highly likely the same. The essentially identical spatial expression patterns and steady-state expression levels of htau between rT2 and rT3 mice further validate their appropriateness as models in this study.

We confirmed the presence of an age-dependent impairment of cognition and significant neurodegeneration (as indicated by hippocampal PCL and GCL volumes and brain weights) induced by tTA/htau P301L expression in rT2 mice and investigated the impact of the Casp2 cleavage-resistant D314E mutation using

rT3 mice. In examining various pathologic tau markers (AT8, CP13, MC1, and PHF-1), we found no difference in signal number or intensity between these lines of mice. It is important to note that, while at 8 months of age cognition was impaired in rT2 but not rT3 mice, there was no difference in the relative levels of the pathologic tau markers. In addition, while at 12 months of age hippocampal CA1 integrity (as indicated in PCL volume measurements) was reduced in rT2 relative to rT3 mice, and at 15 months of age brain weights were reduced in rT2 relative to rT3 mice, these reductions were not accompanied by differences in the relative levels of pathologic tau in rT2 compared with rT3 mice. Overall, our results indicate that the phosphorylation and accumulation of tau in the somatodendritic regions of neurons are not associated with either cognitive impairment or neurodegeneration in this model system, and that the protective effects of the D314E mutation on spatial memory and neurodegeneration occur independent of these processes. These results are consistent with previous reports describing the dissociation of neurofibrillary tangles and phosphorylated tau from cognitive function, synaptic function, and neuronal integrity (Santacruz et al., 2005; de Calignon et al., 2010; Rocher et al., 2010; Sydow et al., 2011; Crimins et al., 2012; Kuchibhotla et al., 2014; Rudinskiy et al., 2014).

Interestingly, although we identified a protective effect of the D314E mutation on spatial memory, the effect is present at 8 but not 12 months of age. In view of this delayed occurrence of memory deficits in rT3 relative to rT2 mice, we postulate that site-specific htau cleavage at D314 may contribute to dementia primarily at the earliest stages of disease. In support of this result, we found that levels of Δtau314 are highest in the brain of elderly individuals with mild cognitive impairment, compared with age-matched, cognitively normal individuals and individuals with AD (P.L., K.H.A. et al., unpublished observations).

Our data reveal that memory deficits are closely associated with tau accumulation and AMPAR loss in PSD. Together with the observed transient memory protection by the cleavage-resistant mutation, these findings lend substantial support to the hypothesis that htau cleavage at D314 drives tau into dendritic spines and disrupts early cognitive dysfunction. This cleavage process triggers the de-anchoring of surface AMPAR and induces abnormal synaptic transmission, as shown previously (Zhao et al., 2016; Teravskis et al., 2020). We have yet to understand the specific mechanism by which htau cleavage at D314 promotes the entry of tau to dendritic spines. One possibility is related to the observation that the FTD-linked htau P301L variant contributes to pathogenesis through enhancing oligomer formation (Maeda et al., 2018) and that the water-inaccessible core of formed oligomers contains truncated tau fragments lacking the C-terminal microtubule-binding domain (Aoyagi et al., 2007). In addition, Δtau314 aggregates are a nonfibrillar species (Zhao et al., 2016). Casp2 has also been to shown to localize at the base of dendritic spines in a mouse model of AD (Pozueta et al., 2013). Given these findings, we hypothesize that Δtau314 is produced locally in dendritic spines, and these fragments serve as nucleation seeds that promote tau oligomerization and accumulation. In order to validate these hypotheses, future studies will focus on understanding the occurrence of Casp2 cleavage of tau in synapses and the biochemical and biophysical properties of Δtau314 aggregates under pathophysiological conditions. Meanwhile, it is worth noting that other tau-related, cognition-affecting mechanisms have been found to be relevant in FTD, for example, tau oligomerization (Lasagna-Reeves et al., 2011),

asparagine endopeptidase-mediated tau cleavage (Zhang et al., 2014), and site-specific tau acetylation (Tracy et al., 2016). While the intrinsic connection between these identified molecular events remains largely unexplored, an alteration in AMPAR trafficking in dendritic spines may be involved in the detrimental effects of both htau cleavage at D314 and tau acetylation (Tracy et al., 2016; Zhao et al., 2016). As such, these pathogenic pathways may be interrelated, and early cognitive deterioration mediated by htau cleavage by Casp2 may be augmented by other mechanisms during disease progression.

It was recently shown that expressing WT htau in targeted-insertion rT1 mice for the first month of life leads to more severe brain atrophy than expressing htau P301L in age- and genetically matched rT2 mice, and that this is likely because of greater phosphorylation and slower clearance of WT htau during development (Gamache et al., 2020). We found that such WT htau-associated neurodevelopmental toxicity persists until at least 5 months of age (Fig. 7), as brain weights of rT1 mice remain lower than rT2 mice. Starting in middle age (i.e., 12-15 months), we observed brain weight loss in all three transgenic lines compared with their non-Tg littermates. While this likely reflects a transgene overexpression effect, rT2 mice showed a greater reduction in brain weight and hippocampal CA1 volume than age-matched rT1 mice. This indicates that the FTD-associated htau P301L variant induces age-related neurodegeneration in developmentally mature animals and supports the use of rT2 paired with rT1 mice to study the pathogenesis of FTD.

The Casp2 cleavage-resistant D314E mutation temporarily alleviates hippocampal neurodegeneration and brain atrophy, which is consistent with a previous AAV model showing that the mutation prevents htau P301L-induced hippocampal volume reduction (Zhao et al., 2016). The exact mechanism underlying the neuroprotective effects of the D314E mutation is presently unclear but is likely through modulating both apoptosis pathways and senescence-associated molecular phenotypes (P.L., unpublished findings). Nonetheless, this study substantiates a novel tau-elicited neurodegenerative mechanism of FTD, and joins a multitude of known mechanisms, including the roles of tau in TANK-binding kinase 1 interaction (Abreha et al., 2021), receptor CB2 expression induction (Galan-Ganga et al., 2021), calpain-mediated signaling activation (Rao et al., 2014), BDNF expression reduction (Jiao et al., 2016), cell cycle reentry promotion (Jaworski et al., 2009), and PERK signaling dysregulation (Radford et al., 2015). We are also striving to understand how Casp2 cleavage of htau at D314 causes neurodegeneration and behavioral abnormalities in other types of tauopathies in which nonmutant tau drives pathology, such as AD and Lewy body dementia. Understanding the role of this cleavage event as it pertains to different neurologic diseases may facilitate the development of effective therapeutic strategies to combat specific illnesses.

In conclusion, this study improves our understanding of the role of Casp2-mediated htau cleavage at D314 in FTD pathogenesis. For the first time, we show that blocking htau cleavage transiently protects against age-related memory impairment and neurodegeneration, and we verify the effects of this cleavage on postsynaptic tau accumulation and AMPAR de-anchoring in the brain. These findings add knowledge to tau-mediated pathologic mechanisms of FTD and guide the development of dementia therapies.

References

Abreha MH, Ojelade S, Dammer EB, McEachin ZT, Duong DM, Gearing M, Bassell GJ, Lah JJ, Levey AI, Shulman JM, Seyfried NT (2021) TBK1 interacts with tau and enhances neurodegeneration in tauopathy. J Biol Chem 296:100760.

Alshammari TK, Alshammari MA, Nenov MN, Hoxha E, Cambiaghi M, Marcinno A, James TF, Singh P, Labate D, Li J, Meltzer HY, Sacchetti B, Tempia F, Laezza F (2016) Genetic deletion of fibroblast growth factor 14 recapitulates phenotypic alterations underlying cognitive impairment associated with schizophrenia. Transl Psychiatry 6:e806.

Aoyagi H, Hasegawa M, Tamaoka A (2007) Fibrillogenic nuclei composed of P301L mutant tau induce elongation of P301L tau but not wild-type tau. J Biol Chem 282:20309–20318.

Ballatore C, Lee VM, Trojanowski JQ (2007) Tau-mediated neurodegeneration in Alzheimer's disease and related disorders. Nat Rev Neurosci 8:663–672.

Beard C, Hochedlinger K, Plath K, Wutz A, Jaenisch R (2006) Efficient method to generate single-copy transgenic mice by site-specific integration in embryonic stem cells. Genesis 44:23–28.

Bodea LG, Eckert A, Ittner LM, Piguet O, Gotz J (2016) Tau physiology and pathomechanisms in frontotemporal lobar degeneration. J Neurochem 138 Suppl 1:71–94.

Cook C, Kang SS, Carlomagno Y, Lin WL, Yue M, Kurti A, Shinohara M, Jansen-West K, Perkerson E, Castanedes-Casey M, Rousseau L, Phillips V, Bu G, Dickson DW, Petrucelli L, Fryer JD (2015) Tau deposition drives neuropathological, inflammatory and behavioral abnormalities independently of neuronal loss in a novel mouse model. Hum Mol Genet 24:6198–6212.

Cook-Snyder DR, Jones A, Reijmers LG (2015) A retrograde adeno-associated virus for collecting ribosome-bound mRNA from anatomically defined projection neurons. Front Mol Neurosci 8:56.

Crimins JL, Rocher AB, Luebke JI (2012) Electrophysiological changes precede morphological changes to frontal cortical pyramidal neurons in the rTg4510 mouse model of progressive tauopathy. Acta Neuropathol 124:777–795.

de Calignon A, Fox LM, Pitstick R, Carlson GA, Bacskai BJ, Spires-Jones TL, Hyman BT (2010) Caspase activation precedes and leads to tangles. Nature 464:1201–1204.

de Calignon A, Polydoro M, Suarez-Calvet M, William C, Adamowicz DH, Kopeikina KJ, Pitstick R, Sahara N, Ashe KH, Carlson GA, Spires-Jones TL, Hyman BT (2012) Propagation of tau pathology in a model of early Alzheimer's disease. Neuron 73:685–697.

Deyle DR, Russell DW (2009) Adeno-associated virus vector integration. Curr Opin Mol Ther 11:442–447.

Di Re J, Wadsworth PA, Laezza F (2017) Intracellular fibroblast growth factor 14: emerging risk factor for brain disorders. Front Cell Neurosci 11:103.

Dumanchin C, Camuzat A, Campion D, Verpillat P, Hannequin D, Dubois B, Saugier-Veber P, Martin C, Penet C, Charbonnier F, Agid Y, Frebourg T, Brice A (1998) Segregation of a missense mutation in the microtubule-associated protein tau gene with familial frontotemporal dementia and parkinsonism. Hum Mol Genet 7:1825–1829.

Galan-Ganga M, Rodriguez-Cueto C, Merchan-Rubira J, Hernandez F, Avila J, Posada-Ayala M, Lanciego JL, Luengo E, Lopez MG, Rabano A, Fernandez-Ruiz J, Lastres-Becker I (2021) Cannabinoid receptor CB2 ablation protects against tau induced neurodegeneration. Acta Neuropathol Commun 9:90.

Gamache J, Benzow K, Forster C, Kemper L, Hlynialuk C, Furrow E, Ashe KH, Koob MD (2019) Factors other than hTau overexpression that contribute to tauopathy-like phenotype in rTg4510 mice. Nat Commun 10:2479.

Gamache JE, Kemper L, Steuer E, Leinonen-Wright K, Choquette JM, Hlynialuk C, Benzow K, Vossel KA, Xia W, Koob MD, Ashe KH (2020) Developmental pathogenicity of 4-repeat human tau is lost with the P301L mutation in genetically matched tau-transgenic mice. J Neurosci 40:220–236.

Goodwin LO, Splinter E, Davis TL, Urban R, He H, Braun RE, Chesler EJ, Kumar V, van Min M, Ndukum J, Philip VM, Reinholdt LG, Svenson K, White JK, Sasner M, Lutz C, Murray SA (2019) Large-scale discovery of mouse transgenic integration sites reveals frequent structural variation and insertional mutagenesis. Genome Res 29:494–505.

Han HJ, Allen CC, Buchovecky CM, Yetman MJ, Born HA, Marin MA, Rodgers SP, Song BJ, Lu HC, Justice MJ, Probst FJ, Jankowsky JL (2012) Strain background influences neurotoxicity and behavioral abnormalities in mice expressing the tetracycline transactivator. J Neurosci 32:10574–10586.

Holscher C (1999) Stress impairs performance in spatial water maze learning tasks. Behav Brain Res 100:225–235.

Hoover BR, Reed MN, Su J, Penrod RD, Kotilinek LA, Grant MK, Pitstick R, Carlson GA, Lanier LM, Yuan LL, Ashe KH, Liao D (2010) Tau mislocalization to dendritic spines mediates synaptic dysfunction independently of neurodegeneration. Neuron 68:1067–1081.

Hutton M, et al. (1998) Association of missense and 5′-splice-site mutations in tau with the inherited dementia FTDP-17. Nature 393:702–705.

Jankowsky JL, Slunt HH, Gonzales V, Savonenko AV, Wen JC, Jenkins NA, Copeland NG, Younkin LH, Lester HA, Younkin SG, Borchelt DR (2005) Persistent amyloidosis following suppression of abeta production in a transgenic model of Alzheimer disease. PLoS Med 2:e355.

Jaworski T, Dewachter I, Lechat B, Croes S, Termont A, Demedts D, Borghgraef P, Devijver H, Filipkowski RK, Kaczmarek L, Kugler S, Van Leuven F (2009) AAV-tau mediates pyramidal neurodegeneration by cell-cycle re-entry without neurofibrillary tangle formation in wild-type mice. PLoS One 4:e7280.

Jiao SS, Shen LL, Zhu C, Bu XL, Liu YH, Liu CH, Yao XQ, Zhang LL, Zhou HD, Walker DG, Tan J, Gotz J, Zhou XF, Wang YJ (2016) Brain-derived neurotrophic factor protects against tau-related neurodegeneration of Alzheimer's disease. Transl Psychiatry 6:e907.

Kovacs GG (2015) Invited review: neuropathology of tauopathies: principles and practice. Neuropathol Appl Neurobiol 41:3–23.

Kovacs GG (2017) Tauopathies. Handb Clin Neurol 145:355–368.

Kuchibhotla KV, Wegmann S, Kopeikina KJ, Hawkes J, Rudinskiy N, Andermann ML, Spires-Jones TL, Bacskai BJ, Hyman BT (2014) Neurofibrillary tangle-bearing neurons are functionally integrated in cortical circuits in vivo. Proc Natl Acad Sci USA 111:510–514.

Lasagna-Reeves CA, Castillo-Carranza DL, Sengupta U, Clos AL, Jackson GR, Kayed R (2011) Tau oligomers impair memory and induce synaptic and mitochondrial dysfunction in wild-type mice. Mol Neurodegener 6:39.

Lewis J, McGowan E, Rockwood J, Melrose H, Nacharaju P, Van Slegtenhorst M, Gwinn-Hardy K, Murphy MP, Baker M, Yu X, Duff K, Hardy J, Corral A, Lin WL, Yen SH, Dickson DW, Davies P, Hutton M (2000) Neurofibrillary tangles, amyotrophy and progressive motor disturbance in mice expressing mutant (P301L) tau protein. Nat Genet 25:402–405.

Liu P, Kemper LJ, Wang J, Zahs KR, Ashe KH, Pasinetti GM (2011) Grape seed polyphenolic extract specifically decreases abeta*56 in the brains of Tg2576 mice. J Alzheimers Dis 26:657–666.

Liu P, Paulson JB, Forster CL, Shapiro SL, Ashe KH, Zahs KR (2015a) Characterization of a novel mouse model of Alzheimer's disease–amyloid pathology and unique beta-amyloid oligomer profile. PLoS One 10:e0126317.

Liu P, Reed MN, Kotilinek LA, Grant MK, Forster CL, Qiang W, Shapiro SL, Reichl JH, Chiang AC, Jankowsky JL, Wilmot CM, Cleary JP, Zahs KR, Ashe KH (2015b) Quaternary structure defines a large class of amyloid-beta oligomers neutralized by sequestration. Cell Rep 11:1760–1771.

Liu P, Smith BR, Huang ES, Mahesh A, Vonsattel JPG, Petersen AJ, Gomez-Pastor R, Ashe KH (2019) A soluble truncated tau species related to cognitive dysfunction and caspase-2 is elevated in the brain of Huntington's disease patients. Acta Neuropathol Commun 7:111.

Liu P, Smith BR, Montonye ML, Kemper LJ, Leinonen-Wright K, Nelson KM, Higgins L, Guerrero CR, Markowski TW, Zhao X, Petersen AJ, Knopman DS, Petersen RC, Ashe KH (2020) A soluble truncated tau species related to cognitive dysfunction is elevated in the brain of cognitively impaired human individuals. Sci Rep 10:3869.

Maeda S, Sato Y, Takashima A (2018) Frontotemporal dementia with parkinsonism linked to chromosome-17 mutations enhance tau oligomer formation. Neurobiol Aging 69:26–32.

Maugard M, Doux C, Bonvento G (2019) A new statistical method to analyze Morris water maze data using Dirichlet distribution. F1000Res 8:1601.

Mayford M, Bach ME, Huang YY, Wang L, Hawkins RD, Kandel ER (1996) Control of memory formation through regulated expression of a CaMKII transgene. Science 274:1678–1683.

McCreath KJ, Howcroft J, Campbell KH, Colman A, Schnieke AE, Kind AJ (2000) Production of gene-targeted sheep by nuclear transfer from cultured somatic cells. Nature 405:1066–1069.

Paulson JB, Ramsden M, Forster C, Sherman MA, McGowan E, Ashe KH (2008) Amyloid plaque and neurofibrillary tangle pathology in a regulatable mouse model of Alzheimer's disease. Am J Pathol 173:762–772.

Pozueta J, Lefort R, Ribe EM, Troy CM, Arancio O, Shelanski M (2013) Caspase-2 is required for dendritic spine and behavioural alterations in J20 APP transgenic mice. Nat Commun 4:1939.

Radford H, Moreno JA, Verity N, Halliday M, Mallucci GR (2015) PERK inhibition prevents tau-mediated neurodegeneration in a mouse model of frontotemporal dementia. Acta Neuropathol 130:633–642.

Ramsden M, Kotilinek L, Forster C, Paulson J, McGowan E, SantaCruz K, Guimaraes A, Yue M, Lewis J, Carlson G, Hutton M, Ashe KH (2005) Age-dependent neurofibrillary tangle formation, neuron loss, and memory impairment in a mouse model of human tauopathy (P301L). J Neurosci 25:10637–10647.

Rao MV, McBrayer MK, Campbell J, Kumar A, Hashim A, Sershen H, Stavrides PH, Ohno M, Hutton M, Nixon RA (2014) Specific calpain inhibition by calpastatin prevents tauopathy and neurodegeneration and restores normal lifespan in tau P301L mice. J Neurosci 34:9222–9234.

Rocher AB, Crimins JL, Amatrudo JM, Kinson MS, Todd-Brown MA, Lewis J, Luebke JI (2010) Structural and functional changes in tau mutant mice neurons are not linked to the presence of NFTs. Exp Neurol 223:385–393.

Rudinskiy N, Hawkes JM, Wegmann S, Kuchibhotla KV, Muzikansky A, Betensky RA, Spires-Jones TL, Hyman BT (2014) Tau pathology does not affect experience-driven single-neuron and network-wide Arc/Arg3.1 responses. Acta Neuropathol Commun 2:63.

Sandi C (1998) The role and mechanisms of action of glucocorticoid involvement in memory storage. Neural Plast 6:41–52.

Santacruz K, Lewis J, Spires T, Paulson J, Kotilinek L, Ingelsson M, Guimaraes A, DeTure M, Ramsden M, McGowan E, Forster C, Yue M, Orne J, Janus C, Mariash A, Kuskowski M, Hyman B, Hutton M, Ashe KH (2005) Tau suppression in a neurodegenerative mouse model improves memory function. Science 309:476–481.

Shankar GM, Li S, Mehta TH, Garcia-Munoz A, Shepardson NE, Smith I, Brett FM, Farrell MA, Rowan MJ, Lemere CA, Regan CM, Walsh DM, Sabatini BL, Selkoe DJ (2008) Amyloid-beta protein dimers isolated directly from Alzheimer's brains impair synaptic plasticity and memory. Nat Med 14:837–842.

Smith BR, Nelson KM, Kemper LJ, Leinonen-Wright K, Petersen A, Keene CD, Ashe KH (2019) A soluble tau fragment generated by caspase-2 is associated with dementia in Lewy body disease. Acta Neuropathol Commun 7:124.

Sydow A, Van der Jeugd A, Zheng F, Ahmed T, Balschun D, Petrova O, Drexler D, Zhou L, Rune G, Mandelkow E, D'Hooge R, Alzheimer C, Mandelkow EM (2011) Tau-induced defects in synaptic plasticity, learning, and memory are reversible in transgenic mice after switching off the toxic tau mutant. J Neurosci 31:2511–2525.

Teravskis PJ, Ashe KH, Liao D (2020) The accumulation of tau in postsynaptic structures: a common feature in multiple neurodegenerative diseases? Neuroscientist 26:503–520.

Teravskis PJ, Oxnard BR, Miller EC, Kemper L, Ashe KH, Liao D (2021) Phosphorylation in two discrete tau domains regulates a stepwise process leading to postsynaptic dysfunction. J Physiol 599:2483–2498.

Terwel D, Lasrado R, Snauwaert J, Vandeweert E, Van Haesendonck C, Borghgraef P, Van Leuven F (2005) Changed conformation of mutant tau-P301L underlies the moribund tauopathy, absent in progressive, nonlethal axonopathy of tau-4R/2N transgenic mice. J Biol Chem 280:3963–3973.

Tracy TE, Sohn PD, Minami SS, Wang C, Min SW, Li Y, Zhou Y, Le D, Lo I, Ponnusamy R, Cong X, Schilling B, Ellerby LM, Huganir RL, Gan L (2016) Acetylated tau obstructs KIBRA-mediated signaling in synaptic

plasticity and promotes tauopathy-related memory loss. Neuron 90:245–260.

Wang X, et al. (2013) Loss of sorting nexin 27 contributes to excitatory synaptic dysfunction by modulating glutamate receptor recycling in Down's syndrome. Nat Med 19:473–480.

Weitzner DS, Engler-Chiurazzi EB, Kotilinek LA, Ashe KH, Reed MN (2015) Morris water maze test: optimization for mouse strain and testing environment. J Vis Exp e52706.

Westerman MA, Cooper-Blacketer D, Mariash A, Kotilinek L, Kawarabayashi T, Younkin LH, Carlson GA, Younkin SG, Ashe KH (2002) The relationship between abeta and memory in the Tg2576 mouse model of Alzheimer's disease. J Neurosci 22:1858–1867.

Xiao M, Xu L, Laezza F, Yamada K, Feng S, Ornitz DM (2007) Impaired hippocampal synaptic transmission and plasticity in mice lacking fibroblast growth factor 14. Mol Cell Neurosci 34:366–377.

Zhang Z, Song M, Liu X, Kang SS, Kwon IS, Duong DM, Seyfried NT, Hu WT, Liu Z, Wang JZ, Cheng L, Sun YE, Yu SP, Levey AI, Ye K (2014) Cleavage of tau by asparagine endopeptidase mediates the neurofibrillary pathology in Alzheimer's disease. Nat Med 20:1254–1262.

Zhao X, Kotilinek LA, Smith B, Hlynialuk C, Zahs K, Ramsden M, Cleary J, Ashe KH (2016) Caspase-2 cleavage of tau reversibly impairs memory. Nat Med 22:1268–1276.